ADOLESCENT ALCOHOL EXPOSURE DISRUPTS ASTROCYTE-SYNAPTIC STRUCTURAL AND FUNCTIONAL COUPLING IN THE MALE DORSAL HIPPOCAMPUS

O. Coulter[1,2], C.D. Walker[1,2], T. Carter[1], H.G. Sexton[1,2], J. Denvir[1], W.C. Risher[1], B.J. Henderson[1], and M-L Risher[1,2*]

[1]Department of Biomedical Research, Joan C. Edwards School of Medicine, Marshall University, Huntington, WV 25701, USA

[2]Neurobiology Research Laboratory, Hershel 'Woody' Williams Veterans Affairs Medical Center, Huntington, WV 25704, USA

*corresponding author

Address (O.C., C.D.W., T.C., H.G.S., J.D., W.C.R., B.J.H., M-L.R.)
Joan C. Edwards School of Medicine, Marshall University
Robert C. Bryd Biotechnology Science Center
1700 3rd Avenue
Huntington
WV, 25705
USA

Tele: 304-696-3894 (Risher)
Tele: 304-696-3428 (Coulter)

Abstract (limit 150-250 words):

Adolescence is a window of heightened vulnerability to the neurotoxic effects of binge ethanol exposure. Adolescent intermittent ethanol (AIE) exposure has been shown to induce long-lasting cognitive and behavioral impairments in patients and rodent models that increase the risk of developing alcohol use disorder (AUD). Our previous work shows that these behavioral deficits coincide with persistent dysfunction of astrocytes. Here, we aim to understand how astrocyte-synaptic structural and functional crosstalk are disrupted following AIE to provide better mechanistic understanding of why behavioral impairments persist into adulthood. Male Sprague-Dawley rats received AIE, a variety of adeno-associated viruses encoding astrocyte-specific sensors, and fiber implantation in the dorsal hippocampal (dHipp) for *in vivo* photometry. A subset of rats received hM3D(Gq) to chemogenetically activate astrocytes. Following AIE and a forced abstinence period that allowed growth into adulthood, rats underwent assessment in the contextual fear conditioning (CFC) task with simultaneous fiber photometry recordings. By combining immunohistochemistry (IHC), Stimulated Emission Depletion (STED) microscopy, fiber photometry, chemogenetics, and slice physiology, we show that AIE induces structural and functional decoupling of astrocytes from synapses and astrocyte dysregulation that persists into adulthood. Remarkably, stimulating astrocytic calcium signaling via chemogenetic activation attenuates heightened fear responding and restores gliotransmitter availability. These findings highlight a critical role for astrocyte–synaptic crosstalk in regulating fear learning and underscore the untapped therapeutic potential of targeting astrocytes to improve behavioral outcomes following substance use.

Introduction (limit 1500 words):

In the United States, alcohol use typically begins during adolescence with consumption escalating throughout the early-to-mid-twenties. Approximately 90% of adolescent consumption is considered binge drinking (4 drinks for a female and 5 drinks for a male within a 2-hr period) with over 35% reporting regular consumption[1]. Binge-like consumption during adolescence has been associated with increased risk-taking behavior that can result in the onset of excessive use of illicit drugs and worsen the individual's mental health[2]. Equally problematic are the long-term consequences that can include chronic health issues, the emergence of psychiatric disorders, persistent cognitive deficits, and increased susecptibility to alcohol and substance misuse[3,4,5]. It has been proposed that this is, in part, due to the convergence of binge drinking with ongoing brain development, resulting in maladaptive brain maturation that drives permanent alterations in neuronal function and connectivity[6].

With rodent models of adolescent intermittent ethanol (AIE) exposure, there is growing evidence demonstrating that adolescent binge drinking compromises neuronal function and associated cognitive and emotional regulation[7,8,9,10,11]. Non-neuronal cells, particularly astrocytes, are key modulators for these outcomes by regulating synaptic structure, function, and cognitive behavior[12,13,14,15]. Astrocytes are specialized glial cells that work extensively within the central nervous system (CNS) to maintain extracellular environment concentration[16], provide neuroprotection[17], and influence synaptic transmission[18,19]. Bidirectional communication between astrocytes and synapses is facilitated via the ensheathment of pre- and postsynaptic terminals by peripheral astrocyte processes (PAPs). Appropriate PAP ensheathment of excitatory synapses is critical for maintaining an optimal homeostatic environment. PAP-synaptic proximity has been shown to result in a number of changes within the tripartite synapse that are

critical for their optimal function[20,21,22]. Despite our growing awareness of how this interaction maintains synaptic health and function, the specific role of astrocytes in AIE-induced changes in neuronal function and behavior remain unclear.

Previous work from our lab and others has demonstrated that AIE results in a reduced threshold for long-term potentiation (LTP) and an overall increase in dHipp and other essential regions' neuronal excitability following a period of forced abstinence[20,23]. The increase in neuronal excitability correlates with the chronic upregulation and release of astrocyte secreted factors that are known to interact with neuronal receptors, influencing synaptogenesis and dendritic spine maturity[24]. Interestingly, the expression of astrocyte secreted factors increases during abstinence and coincides with a shift towards a more immature dendritic spine phenotype within the CA1 dorsal hippocampus (dHipp)[20]. Previous work using 3D electron microscopy to reconstruct male adult rat dHipp shows that reduced PAP ensheathment and proximity to local synapses correlates directly to the level of dendritic spine maturation in the adult dHipp, with more immature spines having reduced PAP coverage[25]. These findings, combined with a growing appreciation for the role that astrocytes play in synaptic maturation, regulation, and behavioral outcomes, provide the rationale for investigating the long-term effects of AIE on astrocyte morphology, PAP-synaptic proximity, and neuronal-astrocyte communication in the adult male CA1 dHipp. We hypothesize that the loss of dendritic spine maturity is due to an AIE-induced loss of PAP-synaptic proximity, driving impaired neuronal-astrocyte communication and contributing to the dysregulation of neuronal activity and behavior. We further hypothesize that activation of dHipp astrocyte-targeted Designer Receptors Activated Only Designer Drugs (DREADDs) is sufficient to rescue AIE-induced disruption of hippocampal-dependent behavior and gliotransmission during a contextual fear conditioning task.

METHODS

Animals

All procedures in this study were conducted in accordance with the guidelines of the American Association for the Accreditation of Laboratory Animal Care and the National Research Council's Guide for Care and Use of Laboratory Animals and were approved by the Institutional Animal Care and Use Committee at Marshall University and the Huntington Veterans Affairs Medical Center. 154 male Sprague Dawley rats (Hilltop Lab Animals Inc., Scottdale, PA) were received on postnatal day (PND) 24.

Intermittent Binge EtOH Exposure

Animals received ethanol (EtOH; cat #89125-162; Koptec 190 Proof Pure Ethanol; Avantor; Radnor, PA) or water (H_2O) as previously described[26]. On PND 30, animals received 10 doses of 5 g/kg EtOH (35% w/v in H_2O) or H_2O via intragastric gavage (i.g.) using a two days on, one day off, two days on, two days off intermittent schedule over 16 days. The EtOH dosage was selected to achieve blood ethanol concentrations (BECs) consistent with those reported in adolescent humans during binge drinking episodes[27] and our previous rodent studies[24,26].

Blood Ethanol Concentrations

To minimize potential confounds associated with stress/EtOH interactions, a parallel group of animals (n = 6) received EtOH and were housed with the experimental animals but were only used for blood collection to assess blood ethanol concentrations (BECs). Blood was collected from the lateral saphenous vein 60 min after EtOH administration on the 1st, 2nd, 6th, and last

dose of EtOH administration. Blood samples were centrifuged for 5 min, and serum was collected and stored at −80C. Samples were analyzed in triplicate using an Analox AM1 alcohol analyzer (Analox Instruments LTD, Stourbridge, UK).

AAV Packaging

All plasmids and prepackaged adeno-associated viruses (AAVs) were obtained from Addgene. AAVs containing the PHP.eB capsid were used to generate PHP.eB::AAV.gfaABC1D.Lck.GFP (Addgene plasmid #105598; RRID:Addgene_105598[28]), PHP.eB::AAV.GfaABC1D.GRAB_Ado1.0 (9.62 x 10^{13}; Addgene plasmid #153288; RRID:Addgene_153288[29]), using the methods described previously by[30]. See supplemental methods section for complete packaging details.

The following prepackaged AAVs were also used: AAV5.GfaABC1D.GCaMP6f (Addgene plasmid #52925; RRID: Addgene_52925[31]), AAV5.GFAP.iGluSnFr.WPRE.SV40 (Addgene plasmid #98930; RRID:Addgene_98930[32]) AAV5.GFAP.hM3D(Gq).mCherry (Addgene plasmid #50478, RRID: Addgene_50478; gift from Bryan Roth); and AAV1.hSyn.iGluSnFr.WPRE.SV40 (Addgene plasmid #98929; RRID: Addgene_98929[32]). All adeno-associated viruses (AAVs) containing PHP.eB capsid were generated using methods previously described[30]. HEK 293T/17 cells (cat #CRL-11268; ATCC, Manassas, VA) were grown to ~90% confluency in 150 mm tissue-culture treated dishes (cat # 229650; CELLTREAT, Pepperell, MA) and co-transfected with 68.6 ug pAd-DeltaF (Addgene #112867; RRID: Addgene_112867; gift from James M. Wilson), 137 ug pUCmini-iCAP-PHP.eB (Addgene # 103005; RRID: Addgene_103005[30]) and 34.4 ug PhP.eB::AAV-GfaABC1D-GRAB_Ado1.0 (Addgene # 153288; RRID:Addgene_153288[29]) or AAV

gfaABC1D Lck-GFP (Addgene # 105598; RRID:Addgene_105598[28]). AAVs were precipitated from media harvested after 3 days and 5 days using 40% polyethylene glycol (PEG)/2.5 M NaCl, and the pooled cells were harvested after 5 days in cell lysis buffer (5 M NaCl and 1 M Tris-HCl). The lysate was incubated with 50 U/mL Benzonase nuclease (cat# 70664-3; Millipore, Burlington, MA) at 37 °C for 30 min. and then centrifuged at 4500 rpm for 30 min at 4 °C. AAV was purified from the resulting lysate using an iodixanol step gradient containing 15, 25, 40 and 60% iodixanol in Optiseal tubes (cat# 361625; Beckman, Brea, CA) followed by centrifugation at 58,400 rpm using a Type 70 Ti ultracentrifuge rotor (Beckman, Brea, CA). Following centrifugation, the AAVs were harvested from the 40% layer using a 10 mL syringe and 18-gauge needle, diluted in Dulbecco's phosphate-buffered saline (DPBS; cat# 14287072; Thermo Fisher Scientific, Waltham, MA) and filtered using a 0.2 µm syringe filter. The AAVs were concentrated and buffer-exchanged by 5 rounds of centrifugation using Amicon Ultra Centrifugal 100 kDa Filters (cat# UFC 910008; Millipore, Burlington, MA). The titer was determined using the qPCR methods previously described[33].

Surgical Procedures

On PND 26-27, rats received 0.3 mg/kg intraperitoneal injection (i.p.) of 25% w/v mannitol[26, 34, 35], buprenorphine (1.0ml/kg), and anesthetized with a cocktail of ketamine (30 mg/kg), xylazine (2.5 mg/kg), and acepromazine (0.5 mg/kg). A burr hole was drilled into both hemispheres of the skull, allowing for the bilateral injection of an AAV into the dHipp at the following coordinates, -3.12 mm AP, +/− 2.5 mm ML, -2.4 mm DV (based on the Paxinos atlas). AAVs previously discussed in 'AAV Packaging' were injected at 1 µL using a 28-gauge needle (cat# C313I/SPC;

P1Technologies, Roanoke, VA) and syringe pump (rate: 20ml/min-330uL/sec; cat# 78-0100W; World Precision Instruments; Sarasota, FL) with a dwell time of 10 minutes. The surgical incision was closed with dissolvable, non-continuous, external sutures (cat# 662G; ETHILON® Nylon Suture; Ethicon, Raritan, NJ), and antibiotic ointment was applied to the incision. Animals were allowed to recover on a heating pad until fully awake and mobile before returning to home cage.

Fiber Photometry

A subset of animals (injected with AAV1.hSyn.iGluSnFr.WPRE.SV40 or PHP.eB::AAV.GfaABC1D.GRAB_Ado1.0) used for the fiber photometry study followed by the same surgery preparations as described above, with slight modifications allowing for fiber-optic cannula implantation. After AAV injection, a fiber (1.25 mm ferrule size; 200 µm core diameter; 0.37 NA; Neurophotometrics, San Diego, CA) was implanted into the right dHipp (-3.12 mm anterior/posterior, +/− 2.5 mm medial/lateral, -2.4 mm dorsal/ventral). Dental cement (cat# 525000 A-M Systems Sequim, WA) was used to secure the fiber-optic canula with the addition of bone anchor screws (cat# 51457; 1.59 mm O.D., 3.2 mm long; Stoelting, Wood Dale, IL).
To record astrocyte glutamate (iGluSnFr) and adenosine (GRAB_Ado1.0) activity in awake behaving rats, we used fiber optic photometrics approach (FP3002, Neurophotometrics) controlled via Bonsai [80] (Bonsai, RRID: SCR_017218), while simultaneously recording behavior in multiple tasks. Glutamate and adenosine signaling (iGluSnFr and GRAB_Ado1.0 excitation at 470nm alongside isosbestic controls (415 nm), light extensity at 50uW) were recorded at 30-60 Hz throughout recording sessions and aligned with behavioral activity using Guided Photometry Analysis in Python[79] (GuPPy) developed by Dr. Talia Lerner (all open source). GuPPy facilitated

baseline correction to isosbestic signals and peak amplitude analysis (ΔF/F, (470nm – 415nm)/415nm). We imported behavioral timestamps as 'TTL' signals allowing the alignment of behavior and photometric data. TTLs were associated with differential freezing/darting characteristics and time-locked to determine changes in signaling during these behavioral events.

Immunohistochemistry (IHC)

Slice Preparation

All slices were prepared as previously described[26]. At PND 46 or 72, animals were deeply anesthetized with isoflurane, transcardially perfused with PBS (pH 7.4; cat# P5368, Sigma-Aldrich, St. Louis, MO) for 1 minute, followed by 7 minutes of 4% paraformaldehyde (PFA; cat# 19210, Electron Microscopy Solutions, Hatfield, PA) at a rate of 20 mL/min. Brain tissue was extracted and post-fixed in 4% PFA at 4 °C overnight, followed by 30% sucrose (cat# G5516-1L, Sigma-Aldrich, St. Louis, MO) in PBS at 4 °C for 2-3 days. Brains were then placed in a plastic mold and submerged in a 2:1 solution consisting of 30% sucrose in PBS:OTC freezing compound (Electron Microscopy Sciences, Hatfield, PA), frozen and then stored at -80 °C. The brains were sliced on a cryostat (CM 1950, Leica Biosystems, Richmond, IL) into either 80 µm or 40 µm sections, depending on the experiment, and stored at -20 °C in a cryoprotectant (1:1 glycerol and PBS).

PSD-95, Ezrin, and Bassoon Immunohistochemistry

40 µm slices were rinsed three times in tris-buffered saline (TBS; pH 7.6) in 0.2% triton 100-X (TBS + 0.2% triton 100-X; TBST) and blocked at room temperature for 1 hour in 10% normal

goat serum (NGS; cat# 005-000-121; Jackson Immunolabs, West Grove, PA) and TBST. Slices were incubated overnight in mouse anti-ezrin (1:500; cat# SAB4200806; RRID:AB_3714841; Sigma-Aldrich, St. Louis, MO), guinea pig anti-bassoon (1:500; cat# 141-318; RRID: AB_2927388; Synaptic Systems, Göttingen, Germany), and rabbit anti-PSD-95 (1:350; cat# 51-6900; RRID:AB_2533914; Thermo Fisher Scientific, Waltham, MA) in 10% NGS and TBST at 4 °C. Slices were washed 3 times in TBST then incubated for 2 hours at room temperature in goat anti-guinea pig 488 (1:100; Alexa Fluor cat# A11073; RRID:AB_2534117; Thermo Fisher Scientific, Waltham, MA), goat anti-mouse 594 (1:100; Alexa Fluor cat# A21125; RRID:AB_2535767; Thermo Fisher Scientific, Waltham, MA), and goat anti-rabbit Atto 647N (1:100; cat# 611-156-122; RRID:AB_10893043; Rockland Immunochemicals, Limerick, Pennsylvania) in 10% NGS and TBST. Slices were washed two times in TBST, once in TBS, and mounted on slides with MOWIOL® 4-88 Reagent (cat# 475904-100GM, Millipore, Burlington, MA) containing 1,4-diazobicyclo-2.2.2-octane (DABCO; cat# 8034560100, Sigma-Aldrich, St. Louis, MO). Slides were then left to cure in the dark for 48 hours.

mGluR2/3/5 and GLAST/GLT-1 Immunohistochemistry

80 µm slices were rinsed in PBST (PBS in 0.2% triton 100-X) three times. Slices underwent antigen retrieval as previously described[26, 35, 36]. Following antigen retrieval, slices were then blocked at room temperature for 1 hour with 5% NGS in PBST. Slices were then placed in one of the following primary antibodies combinations in 5% NGS in PBST: rabbit anti-mGluR2/mGluR3 (1:500; cat#PA1-30151; RRID:AB_1958342; Thermo Fisher Scientific, Waltham, MA) and mouse anti mGluR5 (1:500; cat# MA5-27691; RRID:AB_2735273; Thermo Fisher Scientific, Waltham, MA); guinea pig anti-GLT1 (1:1000; cat# AB1783;

RRID:AB_90949; Sigma-Aldrich, St. Louis, MO) and mouse anti-GLAST (1:1000; cat# MABN794; RRID:AB_2811303; Millipore, Burlington, MA). Secondaries were incubated for 6 hours at room temperature with secondary antibodies and 5% NGS in PBST: goat anti-mouse 594 (1:200; Alexa Fluor cat# A21125; RRID:AB_2535767; Thermo Fisher Scientific, Waltham, MA) and goat anti-rabbit 647 (1:200; Alexa Fluor cat# A-21245; RRID:AB_2535813; Thermo Fisher Scientific, Waltham, MA); goat anti-mouse 594 (1:200; Alexa Fluor cat# A21125; RRID:AB_2535767; Thermo Fisher Scientific, Waltham, MA) and Alexa Fluor goat anti-guinea pig 647 (1:200; Alexa Fluor cat# A-11076; RRID:AB_141930; Thermo Fisher Scientific, Waltham, MA). Slices were washed two times in PBST, once in PBS, and mounted on slides with Vectashield containing DAPI (cat# H-1200, Vector Laboratories West Grove, PA, USA), coverslipped, and sealed with nail varnish. Slides were stored at -20 °C.

ENT1/2 and A1R/A2AR Immunohistochemistry

80 µm slices were rinsed in PBST three times (8 min./wash). Slices underwent antigen retrieval as previously described[22,12,13]. Slices were rinsed three times (5 min./wash) in 0.1 M phosphate buffer (PB; 3.1 g/L NaH2PO4, 10.9 g/l Na2HPO4, pH 7.4), transferred to a 10 mM sodium citrate buffer (2.94 g/L C6H9Na3O9, pH 8.5) preheated to 80 °C for 30 minutes (shaking every 10 minutes) , and allowed to cool to room followed by 3 washes (5 min./wash) in 0.1 M PB. Slices were rinsed three times (10 min./wash) with PBST (PBS in 0.2% triton 100-X) for glycerol removal and then blocked at room temperature for 1 hour with 5% NGS in PBST. Slices were then placed in one of the following primary antibodies: rabbit anti-ENT2 (1:500; cat# BS-10550R; RRID:AB_ 3714842; Thermo Fisher Scientific, Waltham, MA); mouse anti-ENT1 (1:500; cat# sc-377283; RRID:AB_3714843; Santa Cruz, Dallas, TX); rabbit anti-A1R (1:500;

cat# PA1-041A; RRID:AB_2222233; Thermo Fisher Scientific, Waltham, MA), or mouse anti-A2AR (1:500; cat# ab79714; RRID:AB_1603112; Abcam, Cambridge, UK). Secondaries were incubated for 6 hours at room temperature with appropriate secondary antibody: goat anti-mouse 594 (1:200; Alexa Fluor cat# A21125; RRID:AB_2535767; Thermo Fisher Scientific, Waltham, MA) and goat anti-rabbit 647 (1:200; Alexa Fluor cat# A-21245; RRID:AB_2535813; Thermo Fisher Scientific, Waltham, MA); goat anti-mouse 594 (1:200; Alexa Fluor cat# A21125; RRID:AB_2535767; Thermo Fisher Scientific, Waltham, MA) and Alexa Fluor goat anti-guinea pig 647 (1:200; Alexa Fluor cat# A-11076; RRID:AB_141930; Thermo Fisher Scientific, Waltham, MA)

Data Acquisition and Processing

Astrocyte Receptors and Transporters Localization

An Olympus FV3000 laser scanning confocal microscope (Olympus, Tokyo, Japan) with an oil-immersion 40x objective was used for image acquisition (1024 × 1024 frame size, 2.3 zoom, 80um thick, optical section depth of 1 µm) of entire astrocytes of interest. A total of 6-8 randomly selected GFP^+ individual astrocytes in CA1 dHipp (2-3 separate brain slices per animal; 5-6 brains/treatment group). The experimenter was blinded to treatment group throughout the imaging and quantification process. AutoQuant X3.1.2 software (Media Cybernetics, Rockville, MD) was used for deconvolution of the raw image files and using default parameters determined by the software algorithm and based on the confocal model, objective, and imaging specifications. Output files were directly imported to Imaris x64 version 10.2.0 (Bitplane, Santa Barbara, CA) for 3D reconstruction and quantification of astrocytes and transporter/receptor localization methods as previously described[37]. Using Imaris, each

individual astrocyte was first isolated from the Lck-GFP background signal using the surface-building feature. The isolated Lck-GFP channel was then further isolated by sampling of neuropil infiltration volume (NIV) from the reconstructed astrocyte (4 NIV ROIs/astrocyte) using methods previously described[36]. Blinded experimenter manually set the threshold for the puncta signal by measuring the fluorescence intensity of unambiguous positive puncta on multiple optical planes. Once the NIV and puncta were isolated, 'the shortest distance to surfaces' was calculated from the NIV and puncta determine whether the co-stained transporters and receptors were located on the surface of the astrocyte (0 µm from the surface) or internalized (-0.7 µm from the surface). These puncta were then divided by the volume of the NIV to calculate the surface-bound receptors/transporters.

STED PAP-synaptic Puncta Analysis and Decoupling

To obtain an overall puncta count, an Olympus FV3000 laser scanning confocal microscope (Olympus, Tokyo, Japan) with an oil-immersion 40x objective was used for image acquisition (1024 × 1024 image size, 15 µm thick, optical section depth 0.33 µm). Raw synapse count was quantified using previously published routines (https://github.com/Eroglu-Lab/Syn_Bot[38]). To assess puncta proximity, a Leica Stellaris 8 stimulated emission depletion (STED) super-resolution microscope (Cat. No. 11507584; Leica Microsystems, Germany) with an oil-immersion 93X objective was used to acquire images (1024 x 1024 image size, 5x zoom, pixels = 25nm) of the pre-, and post-synaptic terminals, and PAP within the CA1 dHipp. Images were imported into Leica LAS X analysis software (RRID:SCR_013673; Leica Microsystems, Wetzlar, Germany). PAP-synaptic proximity was assessed using the line tool to intersect each

puncta of interest creating a peak intensity plot. The following distances between the peak fluorescent intensities were measured: 1) distance between pre- and post-synaptic terminal, to determine changes in pre- and post-synaptic proximity and 2) (distance between PAP-pre-synaptic terminal + distance between PAP-post-synaptic terminal)/2, to determine the average PAP proximity to each synapse. Quantification was conducted using 5-10 colocalization assessments/ROI from 6-10 ROIs/animal from 6 animals/trt grp.

PSD-95, VGLUT1, Ezrin, and Bassoon Puncta Analysis

An Olympus FV3000 laser scanning confocal microscope (Olympus, Tokyo, Japan) with an oil-immersion 40x objective was used for image acquisition (1024 × 1024 image size, 15 µm thick, optical section depth 0.33 µm). Confocal z-stacks of the dHipp were generated consisting of 15 images within each stack. A total of 3 randomly selected image stacks from a randomly selected hemisphere were captured from 3 separate brain slices per animal (4-6 brains/treatment group). Images were analyzed using slight modifications based on[10]. Z-stacks were uploaded into ImageJ 1.53t (NIH, Bethesda, MD). Stacks were then organized into 3 images per folder of optical sections (corresponding to 1 µm total depth) generated from the original z-stack. Raw synapse count was quantified using previously published routines (https://github.com/Eroglu-Lab/Syn_Bot[38].

Physiology Recordings

Glutamate and Calcium Signaling Recordings

At PND 72-76, animals were deeply anesthetized with isoflurane and the whole brain was removed and placed in artificial cerebral spinal fluid (ACSF) consisting of (in mM): 125 mg

NaCl, 1.6 mg KCl, 1.2 mg NaH_2PO_4, 2.4 mg $CaCl_2$, 1.2 mg $MgCl_2$, 18 mg $NaHCO_3$, 11 mg glucose. 350 µm coronal sections were obtained using a Compresstome (Precisionary Instruments, Natick, MA) and slices were transferred to ACSF that was bubbling in carbogen and incubated in a water bath at 32 °C for 1 hour. Individual slices were transferred to the recording stage equipped with a Zeiss Axiocam 702 mono camera and perfused with ACSF at a constant flow rate of 2-4 ml/min maintained at 32 °C. Astrocytes of interest were identified by expression of GFP (GCaMP6f or iGluSnFR). Physiological recordings were collected using methods previously described in 31 with slight modifications. Following slice preparation and GFP^+ astrocyte identification, the tip of a carbon-fiber bipolar microelectrode (cat # MS303-1-B-SPCL; Plastics One, Roanoke, VA) was placed in the CA1 Schaffer Collateral, and baseline fluorescence was recorded from a GFP^+ astrocyte of interest within the CA1 for 10 s prior to Schaffer Collateral stimulation with an A.M.P.I. Master 9 Stimulator (A.M.P.I., Jerusalem, Israel), during stimulation (1 ms pulses at 350 mA with 15 pulses/sec., rate of 60 Hz), and after stimulation for 15 sec. Fluorescent intensity were captured (frame rate = 200 ms) using Zeiss ZEN Pro (Blue edition) version 3.7.97 (Zeiss, White Plains, NY). An ROI was created to isolate GFP^+ (GCaMP6f or iGluSnFR) astrocytes in the field of view of the CA1 dHipp. Individual fluorescence intensities were isolated for 2 s before neuronal stimulation and continued for 10 seconds following the fluorescent response. A simple linear equation was extrapolated from the fluorescence recordings across the 2 s before Schaffer Collateral stimulation. Raw fluorescence was normalized to account for bleaching by calculating the $\Delta F/F$ and determine changes in fluorescent intensity. Data analysis was conducted using custom-written software in MATLAB 2023b (The Math Works, Natick, Massachusetts).

Astrocyte Membrane Potential Recordings

Following the previously described slice physiology preparation with slight modifications, astrocytes of interest were identified by GFP^+ expression, resting membrane potential (~80 mV), and current-voltage properties[38]. Changes in astrocyte membrane potential were recorded following exogenous glutamate release (glutamate puff, 100µM) in the *stratum radiatum*.

Behavioral Assays

Contextual Fear Conditioning

Following the 26-day forced abstinence period, animals underwent a 3-day contextual fear conditioning (CFC) paradigm previously described[39] using Med Associates operant chambers. Following the 26-day forced abstinence period, animals underwent a 3-day contextual fear conditioning paradigm. Animals were habituated in the room for 30 min. prior to testing, followed by 2-min habituation in the fear conditioning chamber (18x18x30 cm), with a grid floor wired to a shock generator surrounded by an acoustic chamber and a high-quality factory-installed camera on the door (Med Associates, Fairfax, VT). After habituation, the animals received a total of 3, 2 s foot shocks (0.5 mA) with an interval of 120 s between each 2 shocks. Activity within the operant chamber was recorded immediately following each foot shock and throughout the subsequent 120 s. On day 2, the fear retention/extinction day, the animals were allowed to habituate in the room for 30 min. The animal was placed in the fear conditioning chamber for 12 min and operant chamber activity was recorded throughout the session. On day 3, the final extinction day, the animals followed the same schedule as day 2 and all activity within the operant chamber was recorded. A total of six treatment-AAV groups underwent behavioral testing 30 min post-administration of clozapine-N-oxide (CNO, 2 mg/kg in 0.5%

DMSO/saline, i.p.) or saline (control). Treatment groups: 1) H_2O + PHP.eB::AAV.gfaABC1D.Lck.GFP + CNO, 2) H_2O + PHP.eB::AAV.gfaABC1D.Lck.GFP + Saline, 3) H_2O + AAV5.GFAP.hM3D(Gq).mCherry + Saline, 4) H_2O + AAV5.GFAP.hM3D(Gq).mCherry + CNO, 5) EtOH + AAV5.GFAP.hM3D(Gq).mCherry + Saline, and 6) EtOH + AAV5.GFAP.hM3D(Gq).mCherry + CNO.

Open Field

Animals were habituated to the testing room for 30 min. Animals were then placed in center of the open field (dimensions: 40 cm × 40 cm; 10 lux). The 10-min session started when animals were placed in the center of the arena. Upon completion, animals were returned to their home cages. Locomotor activity was recorded using Any-maze Video Tracking System Version 7.08 (Any-maze, Wood Dale, IL, United States; RRID: SCR_014289). The thigmotaxis zone was defined as the outer 10 cm of the apparatus, around the edge of the testing box.

Light Dark Box

Animals were habituated to the testing room for 30 min. Animals were placed in the bright chamber of the light dark box (50 lux on the bright side) and allowed to explore both the light and dark chambers for 10 min (box diameters: 50 cm × 50 cm). Locomotor activity was recorded using Any-maze Video Tracking System Version 7.08 (64-bit, Stoelting, Wood Dale, IL, United States; RRID: SCR_014289). Following the 10 min. session, animals were returned to the home cage. Animals were assessed for time spent in each of the two zones. Entry into a zone was counted when the animal was halfway into the designated zone, i.e., the automated software measured from the center of the body mass.

DeepLabCut

Videos were analyzed using body part tracking from DeepLabCut Software (Version 2.3.11)[40, 41] to determine freezing and darting behavior by extracting the x and y coordinates to identify movements of attempting to escape the apparatus. The number of freezing and darting responses for each animal was recorded and exported to an Excel spreadsheet. Freezing was determined by normalizing the y-axis body parts that were lowest on the apparatus and darting was determined by normalizing to the highest on the apparatus to indicate attempted escapes from the box. We averaged movement 10 sec. prior to pre-shock and 2 sec. immediately following post-shock. The pre-and post-foot shocks were defined as: pre-FS1, -FS2, -FS3 versus post-FS1, -FS2, -FS3. Code is available upon request.

Statistical Analysis

Data were compiled using Excel 365 (Microsoft, Redmond, WA) and analyzed using GraphPad Prism Version 9.4.1 (GraphPad Software, San Diego, CA) or custom-written software in MATLAB 2023b (The Math Works, Natick, Massachusetts). A Linear model regression analyses, mixed-effects ANOVA (timepoint x treatment) with a Tukey's post hoc or Student's t-tests were performed, where indicated. Statistical significance was assessed using an alpha level of 0.05. Data are presented as violin plots with individual data points and medians.

RESULTS

AIE Induced Changes in PAPs-Synaptic Proximity

Previous work in our lab has shown that AIE results in a shift towards an immature dendritic spine phenotype in the male rat hippocampus that persists into adulthood[20]. Prior work also found that dendritic spine immaturity is associated with a loss of PAP-synaptic proximity[25]. We previously confirmed a similar association within subregions of the adult male rat cortex following AIE[26]. Here, we aimed to investigate whether the immature dendritic spine phenotype that we previously reported in the adult dHipp following AIE was associated with a loss of PAP-synaptic proximity. For this experiment, animals received AIE from PND 30 to PND 45. A subset of animals were euthanized 24 hr after the 10th/final EtOH dose (PND 46), while another subset continued through a 26-forced day abstinence period (PND 72, Fig. 1a). These tissue collection timepoints coincided with peak withdrawal and adulthood, respectively. BECs were obtained 60 min. after the first and last dose (Fig. 1b) and confirmed to be consistent with human adolescent binge drinking[27] (Mean ± SEM, mg/dL = 190.5 ± 4.742 and 175.47 ± 4.299).

To determine the effects of AIE on PAP-synaptic proximity, dHipp slices were probed with antibodies against presynaptic (Bassoon), postsynaptic (PSD-95), and PAP (Ezrin) markers and visualized with STED microscopy. Measures of pre- and post-synaptic distance and PAP-synaptic distance showed that AIE decreases synaptic distance (p =0.003) and PAP-synaptic distance (p=0.001) during peak withdrawal (t-test, n =5-6 tripartite synapses/rats, n = 6 rats, Fig. 1c-f). Following the forced abstinence period (in adulthood), pre-post-synaptic distance was indistinguishable from H_2O controls (t-test, p=0.330), suggesting that the effects of AIE on synaptic proximity were temporary. Interestingly, PAP-synaptic distance increased during adulthood (t-test, p=0.027) (Fig. 1g, h) demonstrating a protracted loss of PAP-synaptic proximity into adulthood, indicative of PAP-synaptic structural decoupling.

AIE Loss of PAP-synaptic Proximity Is Not Due to a Loss of Synaptic Number

Previous work has shown that AIE followed by a forced abstinence period into adulthood has differential effects on synaptic number and occurs in a subregion-specific manner[24,26,42]. To determine whether PAP-synaptic decoupling in adulthood is a consequence of PAP or synaptic loss, we quantified total PAP (ezrin), presynaptic (Bassoon), and postsynaptic (PSD-95) puncta (t-test, n= 4-5 images/rat, n= 6 rats, Supplemental Fig. 1a, 2a). AIE had no effect on total Ezrin puncta (Supplemental Fig. 2c), Bassoon puncta (t-test, p=0.330; Supplemental Fig. 1b), PSD-95 puncta (t-test, p=0.624; Fig. 2c), or Bassoon/PSD-95 colocalized puncta (t-test, p=0.259; Supplemental Fig. 1e), suggesting that a loss of synapses is not responsible for the loss of PAP-synaptic coupling following AIE.

AIE Disrupts Astrocyte Ca^{2+} *Responsivity to Neuronal Stimulation Despite Increased Glutamate Availability in Adulthood*

Astrocyte ensheathment of synapses via their PAPs is critically important for sustaining homeostatic synaptic activity, and the loss of PAP coverage has been associated with neurological impairments[43]. Astrocytes remove glutamate from the synaptic cleft to prevent excitotoxicity[44], while glutamate interactions with GPCRs located on PAPs facilitates internal Ca^{2+} (iCa^{2+}) propagation, resulting in feedforward ion and gliotransmitter release[45]. Given the importance of PAP-synaptic proximity for these functions, we assessed whether AIE-induced disruption of PAP-synaptic structural coupling was sufficient to impede neuronal-to-astrocyte functional coupling. Therefore, we targeted dHipp astrocytes with a Ca^{2+} sensor (AAV5.GfaABC1D.GCaMP6f) (Fig. 2a-c) and assessed astrocyte iCa^{2+} responsivity in the *stratum radiatum* to Schaffer Collateral stimulation. Animals that received AIE showed a decrease in astrocyte-specific iCa^{2+} responsivity to neuronal stimulation in adulthood (t-test, 4-6

astrocytes/rat, n= 6 rats, p = 0.040; Fig. 2d). To confirm that the loss of astrocyte iCa^{2+} responsivity was due to less availability of glutamate at the PAP membrane as a consequence of the structural decoupling, we targeted dHipp astrocytes with a membrane bound glutamate sensor (AAV5.GFAP.iGluSnFR.WPRE.SV40) and recorded glutamate availability at PAP membranes in the *stratum radiatum* following Schaffer Collateral stimulation (Fig. 3a-d). At baseline, prior to neuronal stimulation, there was no difference in glutamate availability at the PAPs (t-test, 4-6 astrocytes/rat, n= 6 rats, p=0.467; Fig. 3e). However, despite PAP-synaptic decoupling and a reduction in astrocyte iCa^{2+} responsivity to neuronal stimulation, we observed a robust increase in glutamate-PAP interactions (t-test, p =0.026; Fig. 3f) and a slower decay rate (t-test, p=0.030; Fig. 3g), consistent with increased glutamate availability and therefore slower clearance rate. Additionally, this increase in glutamate availability was consistent with overexpression in VGluT1 that would suggest more glutamate release at the synapse (t-test, n=4-6 images/rat, n=6 rats, p<0.001; Supplemental Fig. 2a,b). These data suggest that the loss of astrocyte functional responsivity to neuronal stimulation is not due to an AIE-induced loss of glutamate-PAP interactions.

Astrocyte clearance of glutamate occurs via glutamate transporters (GLAST and GLT1) and while interactions between glutamate and membrane bound G-protein coupled receptors (GPCRs) at the PAPs play a vital role in the initiation of astrocyte iCa^{2+} propagation[45]. Therefore, despite the high availability of glutamate at PAPs following AIE, if there is a coincident loss of membrane-bound glutamatergic receptor availability, this could contribute to the impaired iCa^{2+} responsivity to neuronal stimulation previously observed. Therefore, we assessed whether AIE results in a loss of membrane-bound glutamatergic receptors and transporters on astrocytes. We employed the use of an astrocyte membrane-specific AAV

(AAV5.GfaABC1D.Lck.GFP) to allow full astrocyte morphological reconstruction and co-stained for metabotropic glutamatergic receptors (mGluR2/3 and mGluR5) and glutamate transporters (GLT1 and GLAST), both located on the membrane (Fig. 3h,i) or internalized (Supplemental Fig. 3a,b). Quantification revealed that AIE had no effects on glutamatergic receptor expression (t-test, n=6-8 astrocytes, n=5-6 rats, mGluR2/3, p=0.6196; mGluR5 p=0.2889; Fig. 3j, k) or transporters (t-test, GLT1, p=01328; GLAST, p=0.9273; Fig. 3l, m). These results show that a loss of astrocyte responsivity is not due to lack of astrocyte-specific glutamate receptor or transporter availability, suggesting that lack of astrocyte responsivity is likely due to functional dysregulation of astrocytes.

Astrocytes Increase Astrocyte-Mediated Cation Clearance in Response to AIE

Astrocytes provide homeostatic support at the tripartite synapse through neurotransmitter uptake and the regulation of ion availability[16]. Potassium (K^+) availability is a critical regulator of synaptic activity and, when not appropriately removed by astrocytes, can result in an increase in neuronal depolarization and hyperexcitability[46]. Based on the AIE-induced increase in glutamate availability following Schaffer Collateral stimulation, we next wanted to determine if astrocytic regulation of cations, a measure predominantly driven by K^+ flux, was also dysregulated. To address this question and control for glutamate release, we recorded astrocyte peak current amplitude following glutamate puff (100 μM) in the *stratum radiatum* (Fig. 4 a-c). AIE increased peak current amplitude compared to controls (t-test, n=5-9 astrocytes/rat, n=5 rats, p=0.025; Fig 4d). These results demonstrate that astrocyte-mediated clearance of K^+ ions increases following AIE, which may represent a compensatory response to chronic, excessive glutamate release in adulthood.

Chemogenetic Astrocyte Activation Rescues AIE-Exacerbated Fear Responding in the Contextual Fear Conditioning Paradigm

Previous work demonstrates that AIE can dysregulate dHipp-dependent behavior[47,39,48,49,50] and that these behaviors are likely bidirectionally regulated by astrocyte by an upregulation of astrocyte iCa^{2+} signaling[51,52]. To determine whether restoring astrocyte iCa^{2+} activity is sufficient to recover AIE-induced heightened fear responding in the CFC task, we expressed astrocyte-specific designer receptor activated by designer drugs (DREADDs, AAV5.GFAP.hM3D(Gq).mCherry) in the dHipp and administered clozapine-N-oxide (CNO, 2 mg/kg, i.p.) 30 min. prior to the CFC day 1 (Fig. 5a, b). Freezing and darting behavior was evaluated throughout all 3 sessions using DeepLabCut (Fig. 5c). Additional behaviors were assessed to ensure no off-target effects of CNO (Supplemental Fig. 4).

Acquisition Phase (day 1): Pre- and post-foot shocks were defined as: pre-FS1, -FS2, -FS3 versus post-FS1, -FS2, -FS3. During pre-FS1, there were no baseline differences in freezing behavior when assessed across treatment groups (RM two-way ANOVA, Tukey's multiple comparisons test, n=12 rats, collapsed across 2 cohorts, average $p > 0.05$; Fig. 5d). Post-FS1, AIE animals displayed significantly higher freezing behavior compared to controls (H_2O+SAL vs. AIE+SAL; RM two-way ANOVA, Tukey's multiple comparisons test, p=0.029; Fig. 5d); this AIE effect was attenuated by chemogenetic astrocyte activation (H_2O+CNO vs. AIE+CNO; p=0.062). Despite AIE-induced heightened freezing in response to FS1, when freezing was re-assessed immediately prior to FS2 (i.e., pre-FS2), all animals showed a similar level of baseline freezing (all p's = 0.377– 0.967). During post-FS2, AIE animals showed a trend towards higher freezing behavior when compared to controls (H_2O+SAL vs. AIE+SAL; RM two-way ANOVA,

Tukey's multiple comparisons test, p=0.085); however, there were no differences between all other treatment groups (all p's = 0.599– 0.999). Consistent with the patterns observed at pre-FS1 and pre-FS2, all animals returned to comparable baseline freezing levels by pre-FS3 (all p's = 0.934–1.00). By post-FS3, there were no differences between groups (all p's = 0.246 – 0.996). These data indicate that AIE animals exhibit heightened freezing responses to foot shock, which subsequently normalized as a consequence of the other groups' more gradual increases in freezing across the session. To assess generalized changes in freezing behavior across the session, the data were collapsed across all three foot shocks and changes in % movement, categorized as freezing (<50% movement) and darting (> 50% movement), were assessed between treatment groups (Fig. 5e-h). Once again, during pre-FS1-3, there were no differences between treatment groups (pre-S1-3, all p's =0.484-0.999). During post-FS1-3, AIE animals showed a robust increase in freezing behavior and reduction in darting behavior when compared to controls (RM two-way ANOVA, Tukey's multiple comparisons test, H_2O+SAL vs. AIE+SAL p=0.0011; H_2O+CNO vs. AIE+SAL p=0.003). This effect was significantly attenuated following dHipp astrocyte activation (H_2O+CNO vs AIE+CNO; p=0.214), demonstrating that dHipp astrocyte activation is sufficient to rescue AIE-induced excessive fear responding during CFC acquisition.

Retention and Extinction (day 2) and Extinction (day 3): Despite AIE-induced increased freezing behavior during fear acquisition, there were no differences in retention or extinction during day 2 or 3 (RM two-way ANOVA, Tukey's multiple comparisons test, all p's= 0.124- 1.000). These data show that chemogenetic astrocyte activation selectively attenuates AIE-induced heightened fear responding during CFC acquisition but does not influence fear recall or fear extinction.

Chemogenetic Astrocyte Activation Rescues AIE-Induced Decoupling of Adenosine and Freezing Behavior During the Contextual Fear Conditioning Paradigm

It has been well established that chemogenetic astrocyte activation using hM3DGq+CNO involves the upregulation of astrocyte iCa^{2+}, and that the propagation of this signaling can lead to an array of downstream events[53] (see[54] for review), including the release of the gliotransmitter adenosine: an important modulator of neuronal activity[55] and fear consolidation through Hipp mechanisms[56]. Based on these previous findings, we wanted to determine if the AIE-induced heightened fear responding was associated with a disruption of downstream adenosine signaling and, if so, whether chemogenetic rescue of astrocyte activity is sufficient to recover functional coupling between freezing behavior and adenosine signaling. To address these questions, we co-injected an astrocyte-specific adenosine sensor (AAV-PHP.eB.GfaABC1D.GRAB_Ado1) and astrocyte-specific hM3DGq (AAV5.GFAP.hM3D(Gq).mCherry) into the dHipp and inserted an optical fiber into the same region of the dHipp and administered clozapine-N-oxide (CNO, 2 mg/kg, i.p.) 30 min. prior to the CFC day 1 (Fig. 6a, b). During pre-FS1-3, animals that received H_2O or AIE followed by astrocyte activation (+CNO) showed significantly higher adenosine availability when compared to non-activated (+SAL) groups (RM two-way ANOVA, Tukey's multiple comparisons test, n=6 rats/trt group, H_2O+SAL vs. H_2O+CNO p=0.049; AIE+SAL vs. AIE+CNO p=0.010, Fig. 6c). At post-FS1-3, only AIE+CNO showed persistently higher adenosine availability when compared to AIE+SAL and H_2O+CNO groups (RM two-way ANOVA, Tukey's multiple comparisons test, AIE+SAL vs. AIE+CNO p=0.010; H_2O+CNO vs. AIE+CNO p=0.004). To assess generalized adenosine availability, the data was collapsed across the session. Animals that received AIE+CNO demonstrated visually higher adenosine availability when compared to all other treatment groups but only reached significance when

compared to the AIE+SAL group (one-way ANOVA, Tukey's multiple comparisons test, AIE+SAL vs. AIE+CNO; p=0.033; Fig. 6d). Lastly, we conducted a linear regression to determine the relationship between adenosine availability and freezing behavior across day 1 (Linear regression analysis, reference= H_2O+SAL, model fit=R^2=0.270, Adj. R^2=0.205, F (7,73) =3.940, p=0.001). When animals received H_2O+SAL there was a positive correlation between adenosine availability and freezing behavior; however, this association was decoupled following AIE (AIE+SAL, β= -0.013, SE= 0.004$p < 0.001$, R^2=0.268). In addition to adenosine decoupling following AIE, membrane-bound and internalized adenosine receptor (A2a) and adenosine transporter (ENT2) protein expression were elevated (Supplemental Fig. 5). When AIE animals received astrocyte activation (AIE+CNO), the AIE-induced negative association between adenosine availability and freezing behavior was completely attenuated and indistinguishable from controls (H_2O+CNO, β= 0.530, SE = 0.206, p = 0.012, R^2=0.023; AIE+CNO β = 0.346, SE = 0.220, p = 0.120, R^2=0.106; Fig. 6e). These data show that chemogenetic dHipp astrocyte activation is sufficient to rescue AIE-induced decoupling of adenosine signaling and freezing behavior during fear acquisition.

Chemogenetic Astrocyte Activation and AIE Independently Decouple Glutamate Signaling and Freezing Response with no Additive or Synergistic Effect When Combined

Our findings indicate that chemogenetic activation of astrocytes is sufficient to restore downstream adenosine availability and re-establish its association with freezing behavior during fear acquisition. Building on this demonstration of gliotransmitter functional recovery, we next investigated whether chemogenetic restoration of astrocyte activity could likewise rescue synaptic glutamate signaling disrupted by AIE. To address this question, we co-injected a

neuron-specific glutamate (AAV1.hSyn.iGluSnFr.WPRE.SV40) sensor and an astrocyte-specific hM3DGq (AAV5.GFAP.hM3D(Gq).mCherry) into the dHipp along with optical fiber implantation to obtain fiber photometry measurements during CFC (Fig. 6f, g). Animals received CNO/saline injection 30 min. prior to the CFC day 1.

Acquisition Phase (day 1): Glutamate measurements were collapsed across pre-FS1-3 and post-FS1-3 (Fig. 6h). During pre-FS1-3 (baseline), animals that received AIE followed by astrocyte activation (AIE+CNO) showed significantly higher glutamate availability when compared to the control group (H_2O+CNO) (RM two-way ANOVA, Tukey's multiple comparisons test, n=6 rats/trt group, H_2O+CNO vs. AIE+CNO p=0.017). Post FS1-3, glutamate synaptic availability declined when compared to pre FS1-3; however, there were no differences between treatment groups (all p's = 0.096– 1.0000). To assess general glutamate availability, data were collapsed across the session. Unlike the adenosine experiment, there were differences in glutamate availability across treatment groups (one-way ANOVA, Tukey's multiple comparisons test; all p's=0.415-0.999; Fig. 6i). Lastly, we conducted a linear regression to assess the association between glutamate availability and freezing behavior throughout the session (Linear regression analysis, reference= H_2O+SAL, model fit=R^2=0.205, Adj. R^2=0.125, F (7,70) =2.58, p=0.020). Within the control group (H_2O+SAL), there was a robust negative correlation between glutamate availability and freezing behavior (β= -0.008, SE = 0.002, p = 0.001, R^2=0.319; Fig 6j). However, this association was lost following astrocyte activation and following AIE administration (H_2O+CNO, β= 0.005, SE = 0.004, p = 0.229, R^2=0.034; AIE+SAL, β =0.008, SE = 0.004, p = 0.047 R^2=0.015; Fig. 6j). Interestingly, when AIE and astrocyte activation were combined (AIE+CNO), there were no additive or synergistic effects (AIE+CNO, β=0.006, SE= 0.003, p=0.066, R^2=0.021). Thus, both AIE and astrocyte activation independently uncouple

synaptic glutamate signaling from behavioral output, in contrast to the restored adenosine–behavior coupling observed under astrocyte activation. These results demonstrate that glutamate availability has an inverse relationship with freezing behavior during fear acquisition and that this interaction is disrupted following AIE. Moreover, chemogenetic astrocyte activation is not sufficient to restore the negative association between synaptic glutamate availability and freezing behavior during fear acquisition.

Discussion

The goal of this study was to define how AIE exposure remodels astrocyte-synaptic communication within the dHipp and to link these changes to enduring alterations in fear learning and extinction. We demonstrate that AIE disrupts the structural and functional integrity of the tripartite synapse by driving a persistent loss of PAP-synaptic coupling. This decoupling coincides with reduced astrocyte iCa^{2+} responsivity to neuronal stimulation, despite increased glutamate availability at PAPs, and manifests as exaggerated fear responding during acquisition. Remarkably, selective chemogenetic activation of dHipp astrocytes was sufficient to attenuate AIE-induced heightened fear responses and restore the positive association between adenosine signaling and freezing behavior during fear acquisition. These findings reveal that AIE drives long-lasting astrocyte-specific pathology that persists into adulthood after abstinence, and that this dysfunction remains reversible through targeted modulation of astrocyte activity.

Astrocyte structural plasticity and tripartite remodeling

Astrocytic processes are highly dynamic regulators of the synaptic microenvironment. Their intimate contact with excitatory synapses is essential for maintaining ionic and neurotransmitter

homeostasis and for fine-tuning synaptic efficacy through iCa^{2+}-dependent feedforward signaling. We show that AIE induces biphasic remodeling of PAP-synaptic proximity defined by an early transient increase in proximity followed by a protracted loss of proximity during abstinence. This pattern likely reflects an initial compensatory attempt to stabilize hyperactive circuits, followed by maladaptive withdrawal that compromises tripartite communication. Our findings align with prior work demonstrating that AIE promotes an immature dendritic spine phenotype without major synapse loss[20], suggesting that PAP withdrawal likely destabilizes synaptic structure rather than eliminating synapses entirely. Importantly, the loss of PAP-synaptic coupling mirrors glial remodeling observed across multiple disease domains, including substance use[57], stress[58], Alzheimer's disease[59], and epilepsy[60]. This convergence supports the idea that repeated insult drives persistent astrocytic maladaptive structural plasticity that outlasts the initial exposure and emphasizes an ongoing need to further understand how astrocyte maladaptive remodeling contributes to synaptic dysregulation across a variety of disease states.

Astrocyte hypoactivity and ion-channel adaptation

The protracted loss of PAP-synaptic structural proximity suggests a functional decoupling between neurons and astrocytes. While we did observe a loss of astrocyte iCa^{2+} signaling following AIE, this was despite increased glutamate vesicle transporter expression within the pre-synaptic terminals and glutamate interactions at the PAP, supporting prior reports in AIE models showing maladaptive neuronal hyperexcitability[20,61,62]. In this AIE model, astrocytes appear to counteract this hyperactivity through enhanced K^+ clearance, reflected by increased inward-rectifying currents[63,64,65]. The absence of changes in glutamate receptor or transporter expression points to a fundamental shift in strategy, away from receptor trafficking and toward

ion-channel regulation, as a means of modulating local excitability. To our knowledge, this represents the first evidence that adolescent ethanol exposure produces a long-term functional remodeling of astrocyte physiological responses to neuronal input.

Astrocyte Ca^{2+} hypoactivity as a mechanistic target

Despite increased glutamate availability, astrocytes failed to mount appropriate iCa^{2+} responses following AIE. This pattern mirrors those seen in aging and neurodegeneration[66,67] and suggests that AIE induces a premature or maladaptive "senescent-like" state in astrocytes[68]. Such iCa^{2+} hypoactivity may fundamentally alter astrocyte-neuron bidirectional coordination within the dHipp, impairing the encoding of contextual and fear-related memories (69,70). Indeed, we found that AIE animals exhibited heightened fear responding during acquisition, replicating earlier work[71]. Furthermore, astonishingly, restoring astrocyte iCa^{2+} dynamics via chemogenetic activation is sufficient to attenuate these abnormal cognitive effects. These cognitive effects closely resemble post-traumatic stress disorder (PTSD) where the patient exhibits exacerbated fear response to trauma 'triggers' and fails to recognize a loss of threat[72]. These results provide the first direct evidence that dHipp astrocyte activity contributes to fear responding during the contextual fear conditioning task, and that disruption of astrocyte activity acts as a mediator of AIE-induced behavioral impairment.

Adenosine signaling as a downstream effector of behavioral dysregulation

Fiber photometry revealed a tight coupling between adenosine release and freezing behavior that was abolished by AIE and reinstated through astrocyte chemogenetic activation. These findings suggest that impaired astrocyte iCa^{2+} signaling disrupts purinergic feedforward signaling critical

for adaptive fear responding during acquisition. AIE also increased A2a receptor expression; this finding is particularly interesting since similar upregulation has been associated with increased neuronal excitability and neurodegeneration (reviewed in[73]) as well as behavioral impairments specifically associated with astrocyte Ca^{2+} hypoactivity[74,75]. Together, these findings position adenosine signaling as a downstream effector of astrocyte dysfunction, linking molecular changes at the tripartite synapse to circuit-level hyperexcitability and behavioral dysregulation of fear responsivity.

Broader implications and translational potential

Although chemogenetic activation restored astrocytic activity and corrected AIE-induced behavioral outcomes, it did not fully recover glutamate homeostasis. Dissecting circuit-specific astrocyte-neuron ensembles, particularly those coordinating dHipp-prefrontal cortex communication, will be essential for identifying when and how astrocytes constrain or facilitate adaptive behavior[76,77,78]. Emerging tools, such as real-time fiber photometry-based functional recordings of astrocyte and neuronal activity combined with machine-learning-based behavioral mapping, now offer an unprecedented opportunity to decode these interactions *in vivo*. Collectively, our results establish astrocyte structural and functional plasticity as key determinants of post-AIE circuit remodeling. They extend the concept of "glial pathology" beyond traditional neurodegeneration to include adolescent alcohol exposure as a driver of long-lasting tripartite synapse dysfunction. By revealing that these astrocytic deficits are reversible through targeted activation, this work opens a new therapeutic avenue for normalizing network excitability and improving mental health outcomes after early-life alcohol misuse.

Conclusion

This study identifies astrocyte-specific structural and functional remodeling as a persistent cellular signature of adolescent alcohol exposure. AIE drives enduring decoupling of the tripartite synapse, disrupts astrocytic iCa^{2+} and adenosine signaling, and alters fear-related behavior; yet, these effects remain amenable to astrocyte-targeted intervention. Recognizing astrocytes as active, plastic regulators of neural circuits reframes them from passive supporters to key therapeutic entry points for treating alcohol- and stress-related neuropsychiatric disease.

Acknowledgments

Special thanks to Katherine Reissner (University of North Carolina, Chapel Hill) for the generous gift of AAV.gfaABC1D.Lck.GFP, and Isabella Parsons for her aid in immunohistochemistry staining and Imaris analysis.

Funding

This work was supported by grants from the Department of Veterans Affairs Biomedical Laboratory Research and Development, Career Development Award (BX002505) to MLR; the Veterans Affairs Merit Award (BX005403) to MLR; National Institutes of Health (R21AA030086) to MLR; National Science Foundation (2242771/OIA-2242771 WV-NFT PI: Serafin Research Leads: MLR WCR, BH); National Institutes of Health (2U54GM104942 PI: Hodder). Contents do not necessarily represent the views of the U.S. Department of Veterans Affairs or the United States Government.

REFRENCES

1. Bachman, J., et al., *The Decline of Substance Use in Young Adulthood: Changes in Social Activities, Roles, and Beliefs*. 2014.
2. Meyers, J.L. and D.M. Dick, *Genetic and environmental risk factors for adolescent-onset substance use disorders.* Child Adolesc Psychiatr Clin N Am, 2010. **19**(3): p. 465-77.
3. Rehm, J., *The risks associated with alcohol use and alcoholism.* Alcohol Res Health, 2011. **34**(2): p. 135-43.
4. Volkow, N.D. and C. Blanco, *Substance use disorders: a comprehensive update of classification, epidemiology, neurobiology, clinical aspects, treatment and prevention.* World Psychiatry, 2023. **22**(2): p. 203-229.
5. Brown, S.A., et al., *Neurocognitive functioning of adolescents: effects of protracted alcohol use.* Alcohol Clin Exp Res, 2000. **24**(2): p. 164-71.
6. Koob, G.F. and N.D. Volkow, *Neurobiology of addiction: a neurocircuitry analysis.* Lancet Psychiatry, 2016. **3**(8): p. 760-773.
7. Spear, L.P., *The adolescent brain and age-related behavioral manifestations.* Neuroscience & Biobehavioral Reviews, 2000. **24**(4): p. 417-463.
8. Squeglia, L.M., et al., *Adolescent binge drinking linked to abnormal spatial working memory brain activation: differential gender effects.* Alcohol Clin Exp Res, 2011. **35**(10): p. 1831-41.
9. Macht, V., N. Elchert, and F. Crews *Adolescent Alcohol Exposure Produces Protracted Cognitive-Behavioral Impairments in Adult Male and Female Rats*. Brain Sciences, 2020. **10**, DOI: 10.3390/brainsci10110785.
10. Hou, J., et al., *Adolescent intermittent alcohol exposure induces adult cognitive deficits via disrupting the septo-hippocampal cholinergic projections.* Life Sci, 2025. **377**: p. 123795.
11. Fisher, R.P., et al., *Adolescent binge alcohol exposure accelerates Alzheimer's disease-associated basal forebrain neuropathology through proinflammatory HMGB1 signaling.* Front Aging Neurosci, 2025. **17**: p. 1531628.
12. Cho, W.H., et al., *Hippocampal astrocytes modulate anxiety-like behavior.* Nat Commun, 2022. **13**(1): p. 6536.
13. Lia, A., et al., *Rescue of astrocyte activity by the calcium sensor STIM1 restores long-term synaptic plasticity in female mice modelling Alzheimer's disease.* Nat Commun, 2023. **14**(1): p. 1590.
14. Escalada, P., et al., *Essential Role of Astrocytes in Learning and Memory.* Int J Mol Sci, 2024. **25**(3).
15. González-Arias, C., et al., *Dysfunctional serotonergic neuron-astrocyte signaling in depressive-like states.* Mol Psychiatry, 2023. **28**(9): p. 3856-3873.
16. Kofuji, P. and E.A. Newman, *Potassium buffering in the central nervous system.* Neuroscience, 2004. **129**(4): p. 1045-56.
17. Rossi, D.J., J.D. Brady, and C. Mohr, *Astrocyte metabolism and signaling during brain ischemia.* Nat Neurosci, 2007. **10**(11): p. 1377-86.
18. Takano, T., et al., *Astrocytes and ischemic injury.* Stroke, 2009. **40**(3 Suppl): p. S8-12.
19. Ngezahayo, A., M. Schachner, and A. Artola, *Synaptic activity modulates the induction of bidirectional synaptic changes in adult mouse hippocampus.* J Neurosci, 2000. **20**(7): p. 2451-8.

20. Risher, M.-L., et al., *Adolescent Intermittent Alcohol Exposure: Persistence of Structural and Functional Hippocampal Abnormalities into Adulthood.* Alcoholism: Clinical and Experimental Research, 2015. **39**(6): p. 989-997.
21. Panatier, A., et al., *Glia-derived D-serine controls NMDA receptor activity and synaptic memory.* Cell, 2006. **125**(4): p. 775-84.
22. Thomas, C.I., et al., *Astrocyte coverage of excitatory synapses correlates to measures of synapse structure and function in primary visual cortex.* bioRxiv, 2023.
23. Becker, H.C. and P.J. Mulholland, *Neurochemical mechanisms of alcohol withdrawal.* Handb Clin Neurol, 2014. **125**: p. 133-56.
24. Risher, M.L., et al., *Adolescent Intermittent Alcohol Exposure: Dysregulation of Thrombospondins and Synapse Formation are Associated with Decreased Neuronal Density in the Adult Hippocampus.* Alcohol Clin Exp Res, 2015.
25. Witcher, M.R., S.A. Kirov, and K.M. Harris, *Plasticity of perisynaptic astroglia during synaptogenesis in the mature rat hippocampus.* Glia, 2007. **55**(1): p. 13-23.
26. Walker, C.D., et al., *Diverging Effects of Adolescent Ethanol Exposure on Tripartite Synaptic Development across Prefrontal Cortex Subregions.* Cells, 2022. **11**(19).
27. Donovan, J.E., *Estimated blood alcohol concentrations for child and adolescent drinking and their implications for screening instruments.* Pediatrics, 2009. **123**(6): p. e975-81.
28. Shigetomi, E., et al., *Imaging calcium microdomains within entire astrocyte territories and endfeet with GCaMPs expressed using adeno-associated viruses.* J Gen Physiol, 2013. **141**(5): p. 633-47.
29. Peng, W., et al., *Regulation of sleep homeostasis mediator adenosine by basal forebrain glutamatergic neurons.* Science, 2020. **369**(6508).
30. Challis, R.C., et al., *Systemic AAV vectors for widespread and targeted gene delivery in rodents.* Nat Protoc, 2019. **14**(2): p. 379-414.
31. Haustein, M.D., et al., *Conditions and constraints for astrocyte calcium signaling in the hippocampal mossy fiber pathway.* Neuron, 2014. **82**(2): p. 413-29.
32. Marvin, J.S., et al., *An optimized fluorescent probe for visualizing glutamate neurotransmission.* Nat Methods, 2013. **10**(2): p. 162-70.
33. Aurnhammer, C., et al., *Universal real-time PCR for the detection and quantification of adeno-associated virus serotype 2-derived inverted terminal repeat sequences.* Hum Gene Ther Methods, 2012. **23**(1): p. 18-28.
34. Carty, N., et al., *Intracranial injection of AAV expressing NEP but not IDE reduces amyloid pathology in APP+PS1 transgenic mice.* PLoS One, 2013. **8**(3): p. e59626.
35. Testen, A., et al., *Region-Specific Differences in Morphometric Features and Synaptic Colocalization of Astrocytes During Development.* Neuroscience, 2019. **400**: p. 98-109.
36. Jiao, Y., et al., *A simple and sensitive antigen retrieval method for free-floating and slide-mounted tissue sections.* J Neurosci Methods, 1999. **93**(2): p. 149-62.
37. Baldwin, K.T., et al., *HepaCAM controls astrocyte self-organization and coupling.* Neuron, 2021. **109**(15): p. 2427-2442.e10.
38. Savage, J.T., et al., *SynBot is an open-source image analysis software for automated quantification of synapses.* Cell Rep Methods, 2024. **4**(9): p. 100861.
39. Broadwater, M. and L.P. Spear, *Consequences of ethanol exposure on cued and contextual fear conditioning and extinction differ depending on timing of exposure during adolescence or adulthood.* Behav Brain Res, 2013. **256**: p. 10-9.

40. Nath, T., et al., *Using DeepLabCut for 3D markerless pose estimation across species and behaviors.* Nature Protocols, 2019. **14**(7): p. 2152-2176.
41. Mathis, A., et al., *DeepLabCut: markerless pose estimation of user-defined body parts with deep learning.* Nature Neuroscience, 2018. **21**(9): p. 1281-1289.
42. Healey, K.L., et al., *Effects of adolescent intermittent ethanol on hippocampal expression of glutamate homeostasis and astrocyte-neuronal tethering proteins in male and female rats.* J Neurosci Res, 2021. **99**(8): p. 1908-1921.
43. Blanco-Suárez, E., A.L. Caldwell, and N.J. Allen, *Role of astrocyte-synapse interactions in CNS disorders.* J Physiol, 2017. **595**(6): p. 1903-1916.
44. Mahmoud, S., et al., *Astrocytes Maintain Glutamate Homeostasis in the CNS by Controlling the Balance between Glutamate Uptake and Release.* Cells, 2019. **8**(2).
45. Panatier, A., et al., *Astrocytes are endogenous regulators of basal transmission at central synapses.* Cell, 2011. **146**(5): p. 785-98.
46. Tong, X., et al., *Astrocyte Kir4.1 ion channel deficits contribute to neuronal dysfunction in Huntington's disease model mice.* Nat Neurosci, 2014. **17**(5): p. 694-703.
47. Reitz, N.L., P.T. Nunes, and L.M. Savage, *Adolescent Binge-Type Ethanol Exposure in Rats Mirrors Age-Related Cognitive Decline by Suppressing Cholinergic Tone and Hippocampal Neurogenesis.* Front Behav Neurosci, 2021. **15**: p. 772857.
48. Ehlers, C.L., et al., *Periadolescent ethanol vapor exposure persistently reduces measures of hippocampal neurogenesis that are associated with behavioral outcomes in adulthood.* Neuroscience, 2013. **244**: p. 1-15.
49. Coleman, L.G., Jr., et al., *Adolescent binge ethanol treatment alters adult brain regional volumes, cortical extracellular matrix protein and behavioral flexibility.* Pharmacol Biochem Behav, 2014. **116**: p. 142-51.
50. Swartzwelder, H.S., et al., *Adolescent Intermittent Alcohol Exposure: Deficits in Object Recognition Memory and Forebrain Cholinergic Markers.* PLoS One, 2015. **10**(11): p. e0140042.
51. Adamsky, A., et al., *Astrocytic Activation Generates De Novo Neuronal Potentiation and Memory Enhancement.* Cell, 2018. **174**(1): p. 59-71.e14.
52. Van Den Herrewegen, Y., et al., *Side-by-side comparison of the effects of Gq- and Gi-DREADD-mediated astrocyte modulation on intracellular calcium dynamics and synaptic plasticity in the hippocampal CA1.* Mol Brain, 2021. **14**(1): p. 144.
53. Araque, A., et al., *Calcium elevation in astrocytes causes an NMDA receptor-dependent increase in the frequency of miniature synaptic currents in cultured hippocampal neurons.* J Neurosci, 1998. **18**(17): p. 6822-9.
54. Goenaga, J., et al., *Calcium signaling in astrocytes and gliotransmitter release.* Frontiers in Synaptic Neuroscience, 2023. **Volume 15 - 2023**.
55. Florian, C., et al., *Astrocyte-derived adenosine and A1 receptor activity contribute to sleep loss-induced deficits in hippocampal synaptic plasticity and memory in mice.* J Neurosci, 2011. **31**(19): p. 6956-62.
56. Li, Y., et al., *Activation of astrocytes in hippocampus decreases fear memory through adenosine A(1) receptors.* Elife, 2020. **9**.
57. Siemsen, B.M., et al., *Heroin Self-Administration and Extinction Increase Prelimbic Cortical Astrocyte-Synapse Proximity and Alter Dendritic Spine Morphometrics That Are Reversed by N-Acetylcysteine.* Cells, 2023. **12**(14).

58. Aten, S., et al., *Chronic Stress Impairs the Structure and Function of Astrocyte Networks in an Animal Model of Depression.* Neurochem Res, 2023. **48**(4): p. 1191-1210.
59. Kater, M.S.J., et al., *Electron microscopy analysis of astrocyte-synapse interactions shows altered dynamics in an Alzheimer's disease mouse model.* Front Cell Neurosci, 2023. **17**: p. 1085690.
60. Witcher, M.R., et al., *Three-dimensional relationships between perisynaptic astroglia and human hippocampal synapses.* Glia, 2010. **58**(5): p. 572-87.
61. Swartzwelder, H.S., M.-H. Park, and S. Acheson, *Adolescent Ethanol Exposure Enhances NMDA Receptor-Mediated Currents in Hippocampal Neurons: Reversal by Gabapentin.* Scientific Reports, 2017. **7**(1): p. 13133.
62. Swartzwelder, H.S., et al., *Changes in the Adult GluN2B Associated Proteome following Adolescent Intermittent Ethanol Exposure.* PLOS ONE, 2016. **11**(5): p. e0155951.
63. Nagy, J.I. and J.E. Rash, *Connexins and gap junctions of astrocytes and oligodendrocytes in the CNS.* Brain Research Reviews, 2000. **32**(1): p. 29-44.
64. Bataveljic, D., et al., *Astroglial Kir4.1 potassium channel deficit drives neuronal hyperexcitability and behavioral defects in Fragile X syndrome mouse model.* Nature Communications, 2024. **15**(1): p. 3583.
65. Sibille, J., U. Pannasch, and N. Rouach, *Astroglial potassium clearance contributes to short-term plasticity of synaptically evoked currents at the tripartite synapse.* J Physiol, 2014. **592**(1): p. 87-102.
66. Jiang, R., et al., *Dysfunctional Calcium and Glutamate Signaling in Striatal Astrocytes from Huntington's Disease Model Mice.* J Neurosci, 2016. **36**(12): p. 3453-70.
67. Zarate, S.M., et al., *Aging reduces calreticulin expression and alters spontaneous calcium signals in astrocytic endfeet of the mouse dorsolateral striatum.* npj Aging, 2023. **9**(1): p. 5.
68. Coulter, O.R., C.D. Walker, and M.-L. Risher, *Astrocyte-specific Ca2+ activity: Mechanisms of action, experimental tools, and roles in ethanol-induced dysfunction.* Biochemistry and Cell Biology, 2023. **101**(5): p. 410-421.
69. Lei, Z., et al., *Chemogenetic Activation of Astrocytes in the Basolateral Amygdala Contributes to Fear Memory Formation by Modulating the Amygdala-Prefrontal Cortex Communication.* Int J Mol Sci, 2022. **23**(11).
70. Kim, Y.R., M. Lee, and M.S. Kim, *Astrocytes in Fear Memory Processing: Molecular Mechanisms Across the Amygdala-Hippocampus-Prefrontal Cortex Network.* Cells, 2025. **14**(18).
71. Chandler, L.J., D.T. Vaughan, and J.T. Gass, *Adolescent Alcohol Exposure Results in Sex-specific Alterations in Conditioned Fear Learning and Memory in Adulthood.* Front Pharmacol, 2022. **13**: p. 837657.
72. Gonzalez, P. and K.G. Martinez, *The role of stress and fear in the development of mental disorders.* Psychiatr Clin North Am, 2014. **37**(4): p. 535-46.
73. Lopes, C.R., R.A. Cunha, and P. Agostinho, *Astrocytes and Adenosine A2A Receptors: Active Players in Alzheimer's Disease.* Frontiers in Neuroscience, 2021. **Volume 15 - 2021**.
74. Peyton, L., et al., *In vivo calcium extrusion from accumbal astrocytes reduces anxiety-like behaviors but increases compulsive-like responses and compulsive ethanol drinking in mice.* Neuropharmacology, 2025. **268**: p. 110320.

75. Orr, A.G., et al., *Astrocytic adenosine receptor A2A and Gs-coupled signaling regulate memory.* Nature Neuroscience, 2015. **18**(3): p. 423-434.
76. Williamson, M.R., et al., *Learning-associated astrocyte ensembles regulate memory recall.* Nature, 2025. **637**(8045): p. 478-486.
77. Serra, I., et al., *Astrocyte ensembles manipulated with AstroLight tune cue-motivated behavior.* Nature Neuroscience, 2025. **28**(3): p. 616-626.
78. Delgado, L. and M. Navarrete, *Shining the Light on Astrocytic Ensembles.* Cells, 2023. **12**(9): p. 1253.

FIGURE LEGENDS

Fig 1. Loss of PAP synaptic proximity following AIE in adulthood. **a.** Experimental design of male adolescent rat dosing paradigm: Beginning at PND 30, animals received 5 g/kg of EtOH or H_2O intragastrically (i.g.) on an intermittent, 2 days on, 1 day off, 2 days on, 2 days off, schedule (blue bars). Brains were collected on PND 46, 24-hr after the last dose during peak withdrawal, or after a 26-day abstinence period, on PND 72. **b.** Blood ethanol concentrations (BECs) were assessed throughout the dosing paradigm (shown as *). **c.** STED representative images of dHipp pre-synaptic bassoon (green, top left), post-synaptic PSD-95 (magenta, top center), and PAP terminal marker ezrin (blue, top right). Merged images of the tripartite synapse (bottom left and bottom center) were used to determine the distances between synaptic and PAP puncta resulting in maximum intensity plots. Distances were determined by using the absolute values between the recorded peaks (bottom right). Scale bar= 2 µm, enlarged (bottom center) scale bar= 50 µm. **d.** Representative images of tripartite synapse proximity following peak withdrawal (PND 46) and forced abstinence period (PND 72) in AIE and H_2O exposed animals. Scale bar= 50 µm. **e, f.**

Mean pre-post synaptic distance and mean PAP-synaptic distance during peak withdrawal (PND 46). **g, h.** Same measures as e,f but following the 26-day abstinence period (PND 72). Data are presented as violin plots and include the distribution of individual data points with interquartile ranges; median, minimum, and maximum measures indicated. Analysis: unpaired t-tests, n= 5 images/slide. 5-7 tripartite synapses/image. 3 slices/animal. 6 animals/treatment group.

Fig 2. Impaired astrocyte responsivity to neuronal stimulation after AIE. a. Experimental design. Schematic representation of intracranial injection of the astrocyte-specific Ca^{2+} sensor (AAV5.GfaABC1D.cyto.GCaMP6f) into the dHipp on PND 26. Beginning at PND 30, animals received AIE or H_2O intermittently through PND 45. Brains were collected on PND 72, and acute hippocampal slices were prepared for physiology. A bipolar stimulating electrode was placed in CA1 region of the *Schaffer Collaterals* to induce neuronal stimulation with simultaneous recording of astrocyte-specific Ca^{2+} signaling within the CA1 dHipp. **b.** Representative images demonstrating confirmation of GCaMP6f (green) expression and specificity for astrocytes (GFAP, blue). Scale bar = 125 µm, 2 µm. **c.** Representative images of astrocyte Ca^{2+} signaling before and after *Schaffer Collateral* stimulation following H_2O and AIE, in adulthood. Scale bar = 10 µm. **d** Quantification of GCaMP6f signal shown as $\Delta F/F$ ratio. Data are presented as violin plots representing the distribution of individual data points. Analysis: unpaired t-tests. n = 6-10 astrocytes/animal, 6 animals/treatment group.

Fig 3. AIE-induced decrease in astrocyte responsivity to neuronal stimulation is not due to a lack of glutamate availability at the PAPs or a loss of receptor availability. a. Schematic

representation of intracranial injection of the astrocyte-specific extracellular glutamate release sensor (AAV5.GFAP.iGluSnFr.WPRE.SV40) in the dHipp on PND 26. Beginning at PND 30, animals received AIE or H_2O intermittently through PND 45. Brains were collected on PND 72 and prepared for acute slice physiology. A bipolar stimulating electrode was placed in CA1 region of the *Schaffer Collaterals* to induce neuronal stimulation with simultaneous recording of astrocyte-membrane specific glutamate signaling within the CA1 dHipp. **b.** Representative trace of AIE and control extracellular glutamate release following single neuronal stimulation. **c.** Representative images demonstrating confirmation of iGluSnFR (green) expression and specificity for astrocytes (GFAP, blue) within the dHipp. Scale bar =125 µm, 2 µm. **d.** Representative images of iGluSnFR in astrocytes before and after neuronal stimulation. Scale bar = 10 µm. **e.** Quantification of ΔF/F ratio prior to neuronal stimulation. **f-g**. Quantification of ΔF/F ratio and signal decay rate following neuronal stimulation. **h.** Schematic representation of intracranial injection of the astrocyte membrane-specific adeno-associated virus (AAV5.gfaABC1D.Lck.GFP) in the dHipp on PND 26. **i.** Representative images of astrocyte surface rendering (Lck-GFP, green), mGluR2/3 (magenta), and mGluR5 (blue) in the adult dHipp following AIE. Scale bar= 20 µm, 5 µm. **j-m**. Quantification of membrane-bound glutamate receptor and transporter expression. Data are presented as violin plots representing the distribution of individual data points. Analysis: unpaired t-tests, n = 6-10 astrocytes/animal, 6-8 x 80 µm image stacks/slide, 2 slices/animal, 6 animals/treatment group.

Fig 4. AIE results in increased astrocyte-mediated clearance of K^+ from the tripartite synapse. a. Left, Schematic representation of intracranial injection of the astrocyte membrane-specific adeno-associated virus (AAV5.gfaABC1D.Lck.GFP) in the dHipp on PND 26.

Beginning at PND 30, animals received AIE or H_2O intermittently through PND 45. Brains were collected on PND 72 and prepared for acute slice physiology. Right, Representative image of astrocyte-specific AAV (Lck-GFP, green) and astrocyte excitation of GFP in the CA1 dHipp. **b.** A bipolar stimulating electrode was placed in CA1 region of the *Schaffer Collaterals* to induce neuronal stimulation and measure changes in astrocyte membrane potential following exogenous glutamate release (glutamate puff; 100 μM) in the CA1 dHipp. **c.** Representative trace of membrane potential following 100 uM glutamate puff for 300 ms. **d.** Quantification of astrocyte peak current amplitude. Analysis: unpaired t-tests, n= 6-10 astrocytes/animal, 5 animals/treatment group.

Fig 5. Chemogenetic recovery of astrocyte activity in the dHipp attenuates behavioral deficits in fear learning following AIE. a. Schematic representation of intracranial injection of the astrocyte membrane-specific adeno-associated virus (AAV5.GFAP.hM3D(Gq).mCherry) in the dHipp on PND 26. Beginning at PND 30, animals received AIE or H_2O intermittently through PND 45. Following 26 day forced abstinence period, animals received saline or clozapine-N-oxide (CNO, i.p. 2 mg/kg) to activate astrocytes. After 30 minutes, animals were assessed in a contextual fear conditioning paradigm. Animals were placed in context A and subjected to 3-foot shocks across a 10-minute test period on day 1. On day 2 and 3, animals were placed in context A for 12 min with no foot shocks. **b.** Representative images of the dHipp, DAPI (blue), hM3DGq (magenta), GFAP (green), and colocalization of GFAP+hM3DGq confirming astrocyte specificity of AAV. **c.** Representative images of DeepLabCut output of labeled body parts on the x-y axis of the context box. **d.** Quantification of freezing behavior in

the CFC task (H_2O+SAL (#) vs. AIE+SAL ($); *p = 0.029-0.085;* H_2O+CNO (&) vs. AIE+CNO (@); *p = 0.062-0.574*). **e-f**. Freeze/dart behavior quantification from sessions collapsed across foot shocks from Day 1 of the CFC. **g-h.** Freeze/dart behavior quantification from Days 2 and 3 of the CFC. Analysis: Repeated measures Two-way ANOVA, n = 12 animals/treatment group across 2 separate cohorts. (*p < 0.05* p < 0.001***)

Fig 6. Astrocyte activation rescues adenosine-freezing functional coupling following AIE. a. Schematic representation of intracranial injection of the astrocyte membrane-specific adeno-associated virus (AAV5.GFAP.hM3D(Gq).mCherry + AAVPHP.eB.GfaABC1D.GRAB_Ado1) and a fiber implant in the dHipp on PND 26. Beginning at PND 30, animals received AIE or H_2O intermittently through PND 45. Following 26 day forced abstinence period, animals received saline or clozapine-N-oxide (CNO, 2 mg/kg, i.p.) to activate astrocytes. After 30 minutes, animals were then assessed for cognitive performance in a contextual fear conditioning paradigm along with real-time glutamate or adenosine availability measurements. **b.** Representative images of the dHipp, hM3DGq (magenta), GRAB_Ado1.0 (green), GFAP (blue), and colocalization of GRAB_Ado1.0+hM3DGq confirming astrocyte specificity of AAV and fiber photometry representative trace across day 1 of fear acquisition. **c.** Quantification of the adenosine ΔF/F ratio before and after foot shock: Pre-FS: (# vs. & ;p=0.0499; $ vs. @; p=0.0103) Post FS1-3: ($ vs. @; p=0.0103; & vs. @; p=0.0041). **d.** Quantification of ΔF/F ratio collapsed across the session. **e.** Scatterplot and trendlines comparing adenosine ΔF/F with freezing behavior (H_2O+SAL, β= 0.007, SE= 0.003, p = 0.015, R^2=0.486; AIE+SAL, β=-0.013, SE= 0.004, p < 0.001 , R^2=0.268; H_2O+CNO, β= -0.005, SE = 0.004, p = 0.012, R^2=-0.029; AIE+CNO, β = -0.004, SE = 0.003, p = 0.120, R^2=-0.044). **f.** Schematic representation of intracranial injection of the astrocyte

membrane-specific adeno-associated virus (AAV5.GFAP.hM3D(Gq).mCherry + AAV5.hSyn.iGluSnFr.WPRE.SV40) **g.** Representative images of the dHipp, hM3DGq (magenta), iGluSnFr (green), GFAP (blue), and localization of iGluSnFr and hM3DGq within a dHipp astrocyte and neuron. **h.** Quantification of glutamate availability (ΔF/F ratio) before and after foot shock (&; *p=0.0166*). **i.** Quantification of the glutamate availability (ΔF/F ratio) collapsed across session (*all p's=0.4147-0.9998*). **j.** Scatterplot and trendlines comparing glutamate availability ΔF/F and freezing behavior (H_2O+SAL, β= -0.008, SE = 0.0024, p = 0.001, R^2=0.319; H_2O+CNO, β= 0.005, SE = 0.004, p = 0.229, R^2=0.034; AIE+SAL, β =0.008, SE = 0.004, p = 0.047, R^2=0.015; AIE+CNO, β =0.006, SE = 0.225, p = 0.066, R^2=0.020). Analysis: Repeated measures Two-way ANOVA and Linear Regression Analysis, n = 6 animals/treatment group. (*p < 0.05* p < 0.001***)

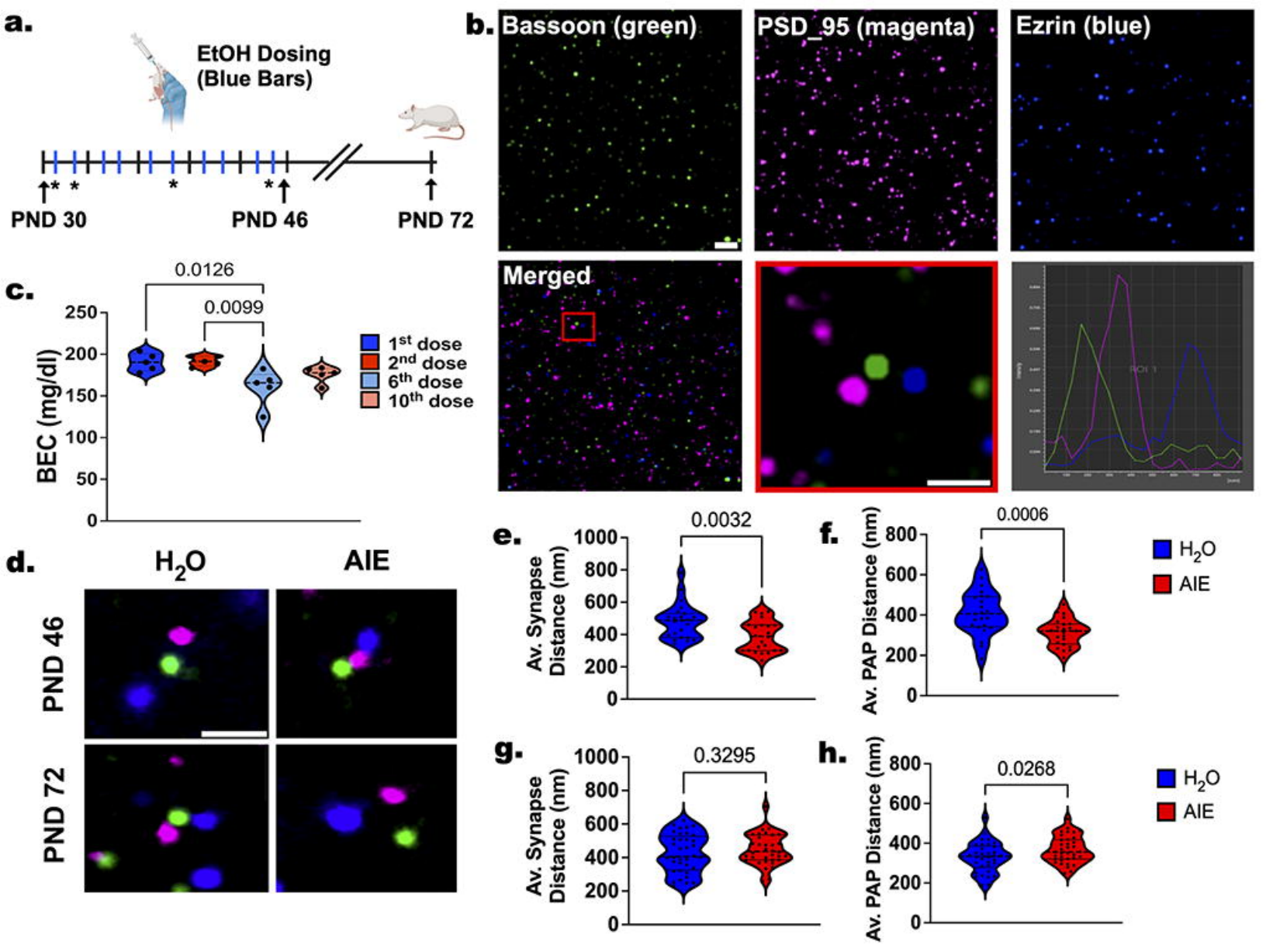
a.
EtOH Dosing
(Blue Bars)
PND 30
PND 46
PND 72
b.
Bassoon (green)
PSD_95 (magenta)
Ezrin (blue)
Merged
c.
0.0126
0.0099
BEC (mg/dl)
250
200
150
100
50
0
1st dose
2nd dose
6th dose
10th dose
d.
H2O
AIE
PND 46
PND 72
e.
0.0032
Av. Synapse Distance (nm)
1000
800
600
400
200
0
f.
0.0006
Av. PAP Distance (nm)
800
600
400
200
0
H2O
AIE
g.
0.3295
Av. Synapse Distance (nm)
1000
800
600
400
200
0
h.
0.0268
Av. PAP Distance (nm)
800
600
400
200
0
H2O
AIE

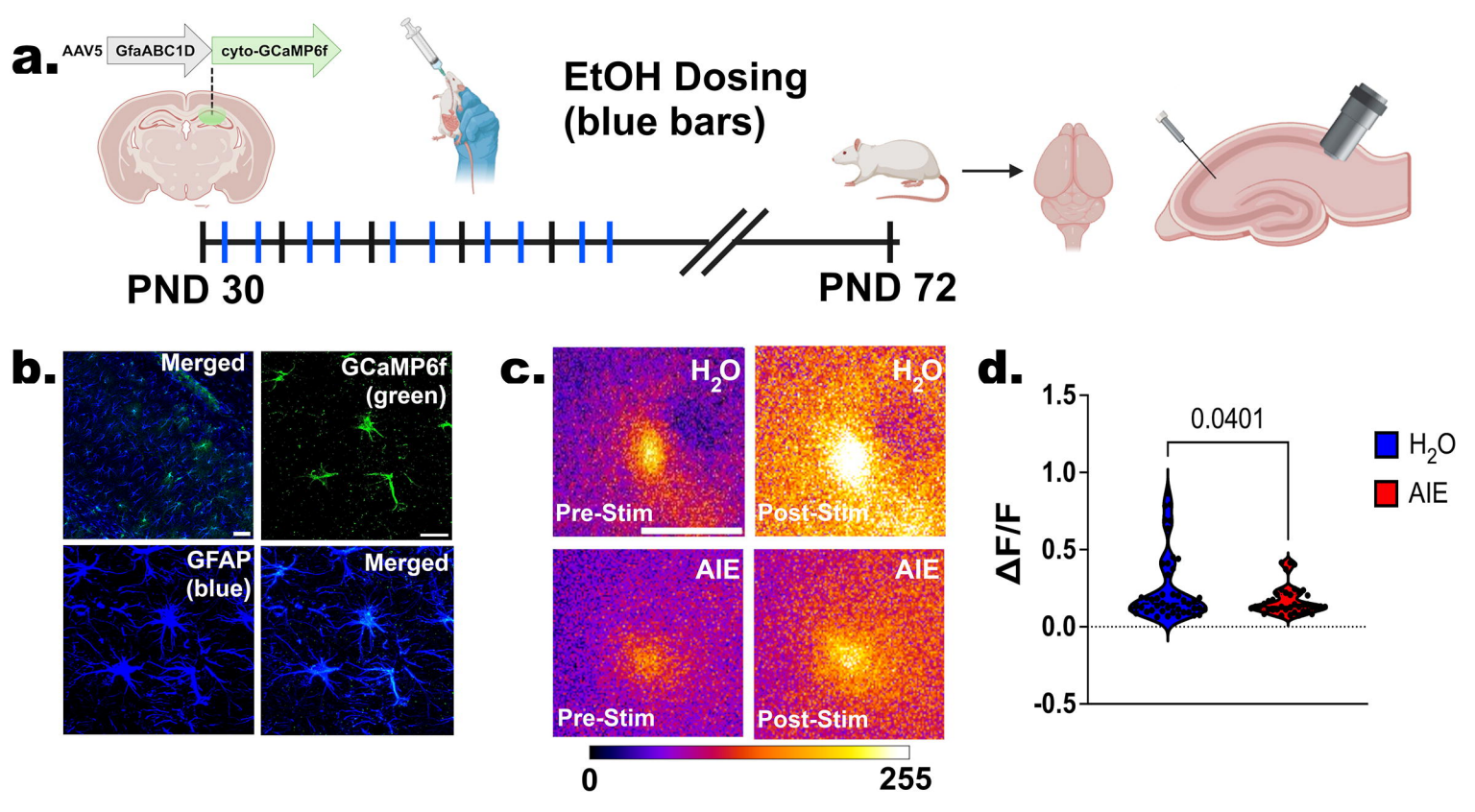
a.
AAV5
GfaABC1D
cyto-GCaMP6f
EtOH Dosing
(blue bars)
PND 30
PND 72
b.
Merged
GCaMP6f
(green)
GFAP
(blue)
Merged
c.
H2O
H2O
Pre-Stim
Post-Stim
AIE
AIE
Pre-Stim
Post-Stim
0
255
d.
1.5
1.0
0.5
0.0
-0.5
ΔF/F
0.0401
H2O
AIE

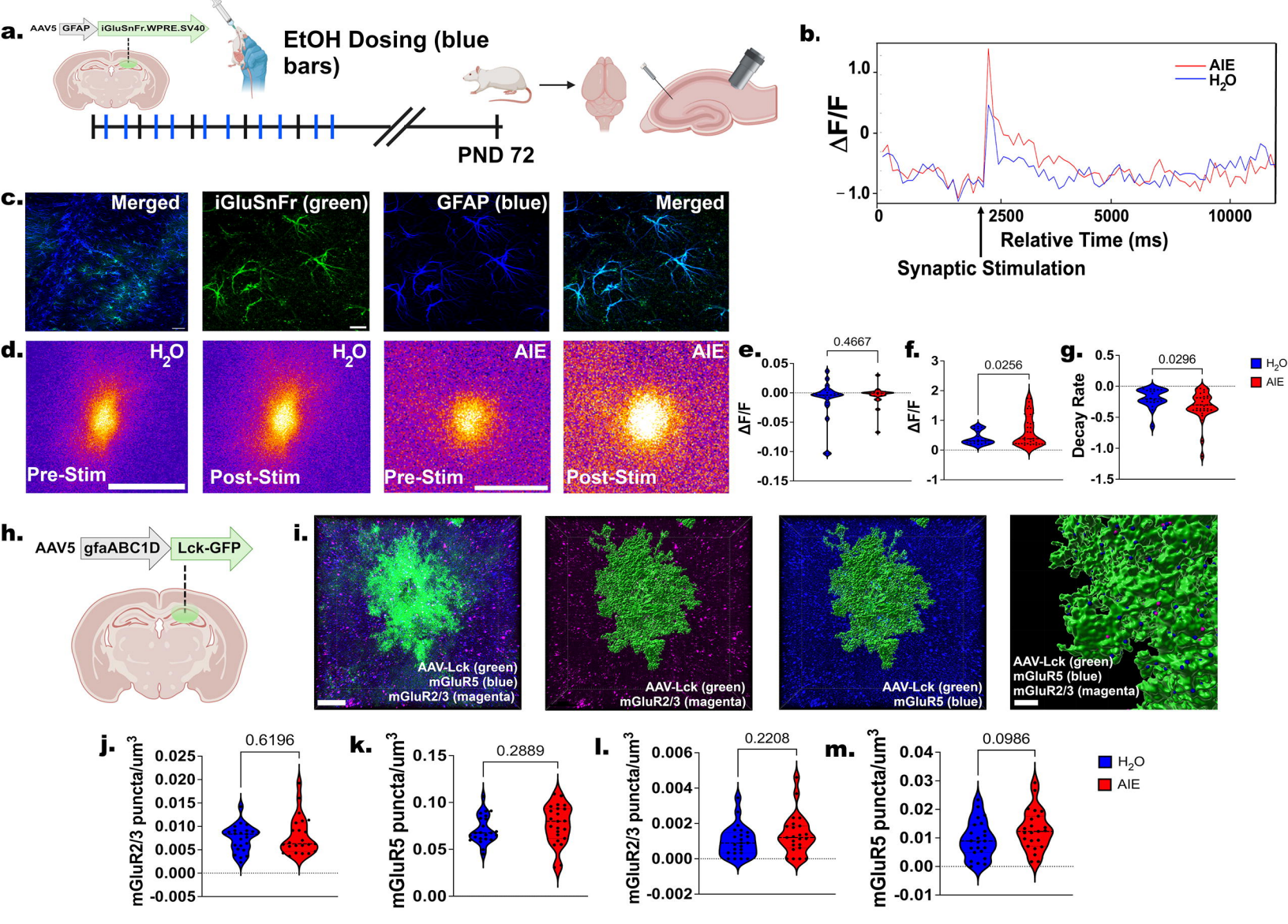
a.
AAV5
GFAP
iGluSnFr.WPRE.SV40
EtOH Dosing (blue bars)
PND 72
b.
AIE
H2O
ΔF/F
1.0
0
−1.0
0
2500
5000
10000
Relative Time (ms)
Synaptic Stimulation
c.
Merged
iGluSnFr (green)
GFAP (blue)
Merged
d.
H2O
H2O
AIE
AIE
Pre-Stim
Post-Stim
Pre-Stim
Post-Stim
e.
0.4667
ΔF/F
0.05
0.00
-0.05
-0.10
-0.15
f.
0.0256
ΔF/F
3
2
1
0
-1
g.
0.0296
Decay Rate
0.5
0.0
-0.5
-1.0
-1.5
H2O
AIE
h.
AAV5
gfaABC1D
Lck-GFP
i.
AAV-Lck (green)
mGluR5 (blue)
mGluR2/3 (magenta)
AAV-Lck (green)
mGluR2/3 (magenta)
AAV-Lck (green)
mGluR5 (blue)
AAV-Lck (green)
mGluR5 (blue)
mGluR2/3 (magenta)
j.
0.6196
mGluR2/3 puncta/um3
0.025
0.020
0.015
0.010
0.005
0.000
-0.005
k.
0.2889
mGluR5 puncta/um3
0.15
0.10
0.05
0.00
l.
0.2208
mGluR2/3 puncta/um3
0.006
0.004
0.002
0.000
-0.002
m.
0.0986
mGluR5 puncta/um3
0.04
0.03
0.02
0.01
0.00
-0.01
H2O
AIE

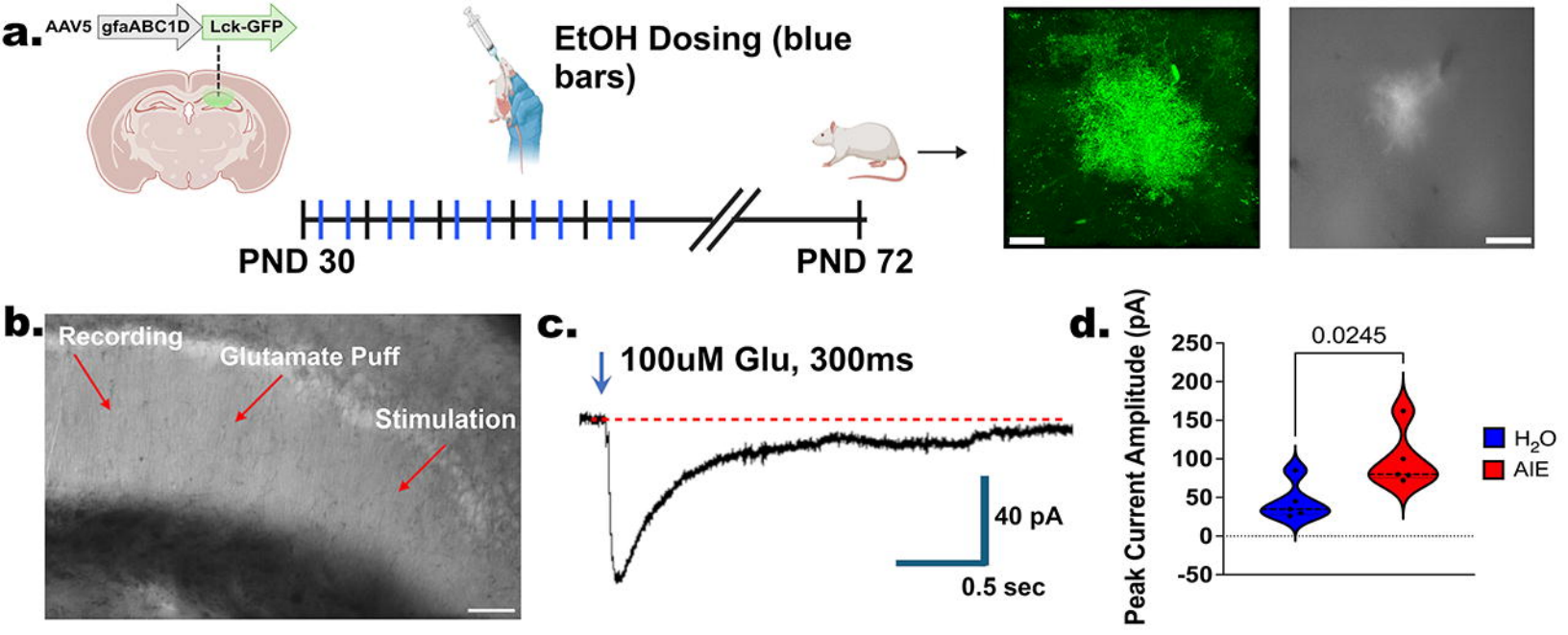
a.
AAV5
gfaABC1D
Lck-GFP
EtOH Dosing (blue bars)
PND 30
PND 72
b.
Recording
Glutamate Puff
Stimulation
c.
100uM Glu, 300ms
40 pA
0.5 sec
d.
Peak Current Amplitude (pA)
0.0245
250
200
150
100
50
0
-50
H2O
AIE

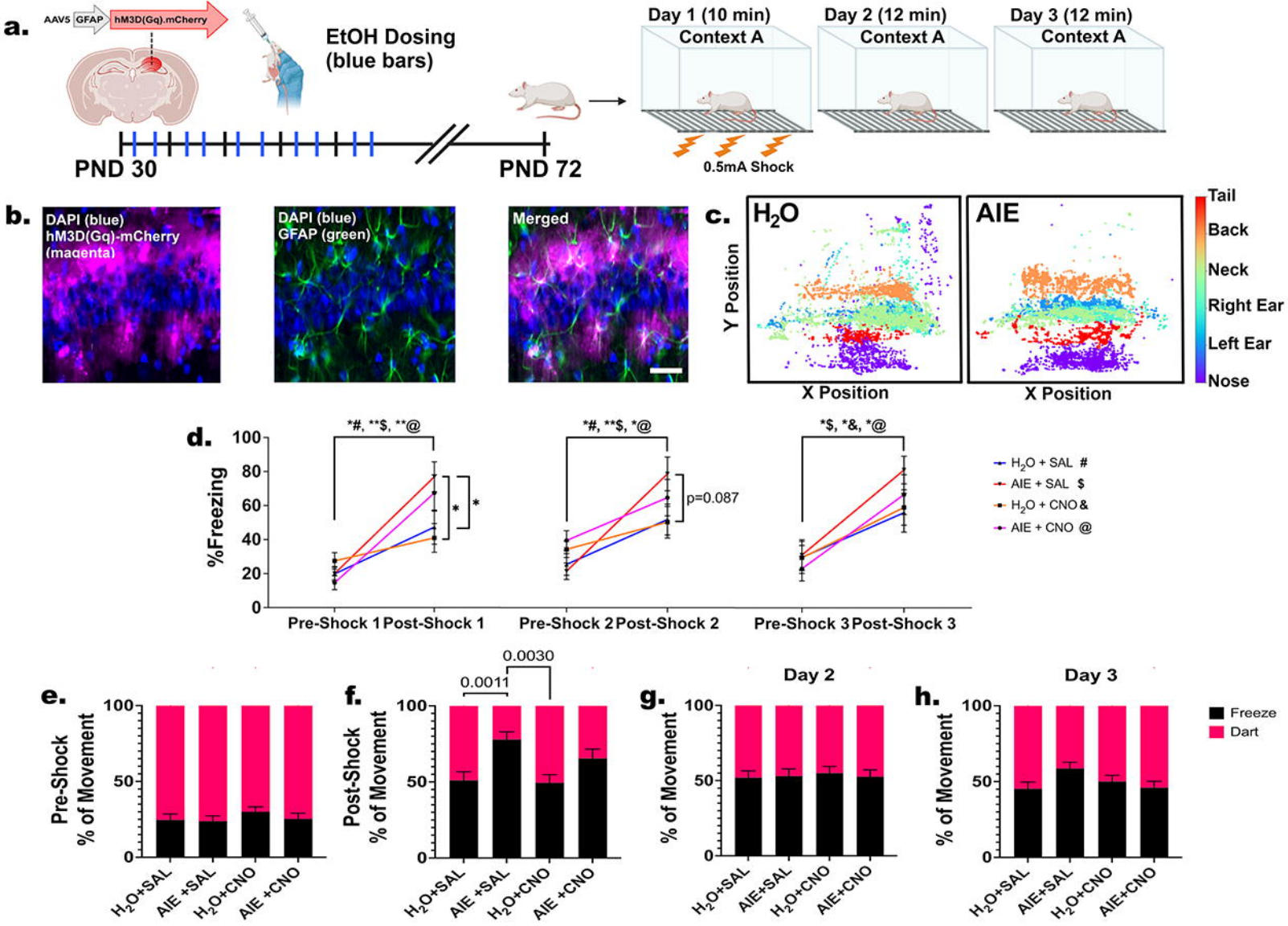
a.
AAV5
GFAP
hM3D(Gq).mCherry
EtOH Dosing
(blue bars)
PND 30
PND 72
Day 1 (10 min)
Context A
Day 2 (12 min)
Context A
Day 3 (12 min)
Context A
0.5mA Shock
b.
DAPI (blue)
hM3D(Gq)-mCherry
(magenta)
DAPI (blue)
GFAP (green)
Merged
c.
H2O
AIE
Y Position
X Position
X Position
Tail
Back
Neck
Right Ear
Left Ear
Nose
d.
%Freezing
*#, **$, **@
*#, **$, *@
*$, *&, *@
p=0.087
Pre-Shock 1
Post-Shock 1
Pre-Shock 2
Post-Shock 2
Pre-Shock 3
Post-Shock 3
H2O + SAL #
AIE + SAL $
H2O + CNO &
AIE + CNO @
e.
Pre-Shock
% of Movement
f.
Post-Shock
% of Movement
0.0011
0.0030
g.
Day 2
% of Movement
h.
Day 3
% of Movement
H2O+SAL
AIE +SAL
H2O+CNO
AIE +CNO
Freeze
Dart

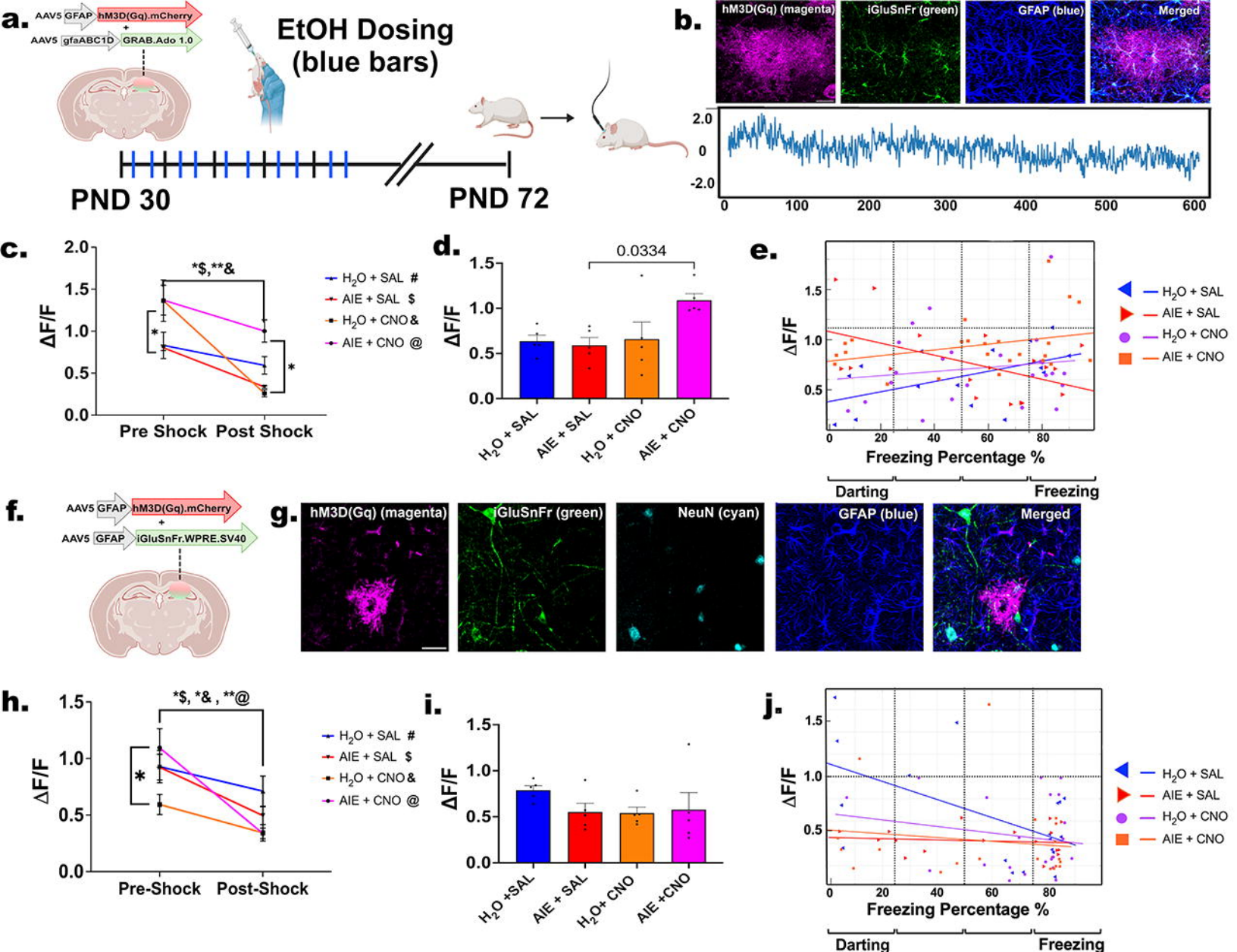
a.
AAV5 GFAP hM3D(Gq).mCherry
+
AAV5 gfaABC1D GRAB.Ado 1.0
EtOH Dosing
(blue bars)
PND 30
PND 72
b.
hM3D(Gq) (magenta)
iGluSnFr (green)
GFAP (blue)
Merged
2.0
0
-2.0
0
100
200
300
400
500
600
c.
*$,**&
ΔF/F
2.0
1.5
1.0
0.5
0.0
Pre Shock
Post Shock
H2O + SAL #
AIE + SAL $
H2O + CNO &
AIE + CNO @
d.
0.0334
ΔF/F
1.5
1.0
0.5
0.0
H2O + SAL
AIE + SAL
H2O + CNO
AIE + CNO
e.
ΔF/F
1.5
1.0
0.5
0
20
40
60
80
Freezing Percentage %
Darting
Freezing
H2O + SAL
AIE + SAL
H2O + CNO
AIE + CNO
f.
AAV5 GFAP hM3D(Gq).mCherry
+
AAV5 GFAP iGluSnFr.WPRE.SV40
g.
hM3D(Gq) (magenta)
iGluSnFr (green)
NeuN (cyan)
GFAP (blue)
Merged
h.
*$, *& , **@
ΔF/F
1.5
1.0
0.5
0.0
Pre-Shock
Post-Shock
H2O + SAL #
AIE + SAL $
H2O + CNO &
AIE + CNO @
i.
ΔF/F
1.5
1.0
0.5
0.0
H2O +SAL
AIE + SAL
H2O+ CNO
AIE +CNO
j.
ΔF/F
1.5
1.0
0.5
0
20
40
60
80
Freezing Percentage %
Darting
Freezing
H2O + SAL
AIE + SAL
H2O + CNO
AIE + CNO